Apparent Hack's Law in River Deltas

Tian Y. Dong[1*], Lawrence Vulis[2], Hongbo Ma[3*], Alejandro Tejedor[4,2], Timothy A. Goudge[5]

Affiliations:

[1]School of Earth, Environmental, and Marine Sciences, University of Texas Rio Grande Valley, Edinburg, USA

*Corresponding author. Email: tian.dong@utrgv.edu

[2]Department of Civil and Environmental Engineering, University of California Irvine, USA

[3]Department of Civil and Environmental Engineering, Ven Te Chow Hydrosystems Laboratory, University of Illinois at Urbana-Champaign, Urbana, USA

*Corresponding author. Email: hongboma@illinois.edu

[4]Institute for Biocomputation and Physics of Complex Systems (BIFI), Universidad de Zaragoza, 50018 Zaragoza, Spain

[5]Department of Earth and Planetary Sciences, Jackson School of Geosciences, The University of Texas at Austin, Austin, USA

Abstract: River deltas are densely populated, ecologically vital landscapes threatened by rising sea levels. Distributary channel networks disperse sediment to build deltaic land, yet the relationship between the organization of distributary networks and deltaic land-building remains elusive. Inspired by Hack's law, which shows that watershed drainage area scales with channel length in tributary networks, we analyzed a global dataset of distributary networks and found a nearly identical scaling relationship between distributary channel length and nourishment area, the land-building counterpart to drainage area. Despite this apparent global scaling, we further identified two distinct local land-building patterns: Uniform Delta Networks consistently follow Hack's law, while Composite Delta Networks exhibit a scale break, transitioning from space-filling growth around the delta apex to quasi-linear growth near the coast. The unexpected growth patterns suggest that global simplicity and local variability coexist in how river deltas grow and organize.

Main Text:

River deltas are densely populated landscapes with critical socioeconomic and ecological functions (*1–4*), hosting ~4.5% of the world's population in only 0.5% of its land area (*5*). However, human and natural forcings, such as upstream damming and rising sea levels, have negatively impacted land building in deltas (*6–10*). Distributary channel networks, widely found in river deltas, enable the dispersal of sediment and organic matter from the upstream river to a much larger area downstream, building deltaic land (*9–14*). The deltaic region where sediment accumulates, downstream of a network apex, is known as a nourishment area (*11–13*), counterpart to the drainage area in tributary basins, where flow accumulates (Fig. 1a). Distributary channels and islands within nourishment areas are mainly built through processes like over-levee floods and channel branching (*15–18*). Whereas it is straightforward to hypothesize that the network organization is linked to land-building, the quantitative relationship between distributary characteristics, such as channel length and nourishment area, is not well understood, even though such a relationship could serve as a helpful rule of thumb for land-building estimation. Prior research has sought to scale the nourishment area (A) with the longest distributary channel length (L) (*11, 13*), primarily based on numerical models. The scarcity of field observations has limited our understanding of the network–nourishment relationship. Delineating A in low-lying environments, such as deltas, is challenging, even with topographic data (Fig. 1a) (*11, 12*). This is because low-relief topography makes the boundaries between neighboring nourishment areas extremely subtle. Such boundaries are theorized to be set by the merging of over-channel, divergent flows in interchannel island areas (*12*), rendering them difficult to measure globally (*19*).

In contrast, a scaling relationship is well-established in geometrically similar tributary channel networks (Fig. 1a): Hack's law (*20, 21*) defines a power law relation between the length of the longest tributary river (L_t) and the area of the associated drainage basin (A_t), $L_t = \alpha A_t^h$. Hack (*20*) observed α =1.4 and h = 0.6 for tributary river networks along the U.S. East Coast, whereas subsequent studies (*22*) have shown h values ranging from 0.5 to 0.7, influenced by basin size (22) and shape (*23*), geology (*23*), and climate (*24, 25*). Geometrically, h = 0.5 indicates space-filling growth, where the channel network grows evenly in both the down and cross (transverse) valley directions (*20–24*). In contrast, $h > 0.5$ indicates preferential down-valley growth, forming elongated basins (20–*24*). Moreover, the case when $h \sim 1$ indicates a linear relationship between channel length and basin area (*20–22*). Although theoretical explanations for Hack's law span concepts ranging from directed random walks (*22*) to optimal network theory (*21, 26*), its physical controls remain debated and have been attributed to internal factors like channel erosional processes via sediment transport (*27*) and external factors (*22*), such as tectonic history (*28*).

Numerous efforts have been made to understand the land-building processes of river deltas through mechanisms such as over-levee flow dispersion (*15*), channel branching and avulsion (*16–18*), and metrics like shoreline roughness (*29*). Yet, despite the geometric parallels between distributary and tributary networks, existing relations between the distributary network (approximated by L) and the nourishment area remain inconclusive (*11, 13*), largely because these relations are based on only two small-scale field deltas (< 150 km^2 in area; mean h = 0.53) (*11*). Moreover, numerically simulated and laboratory-scale deltas yield different scaling exponents (mean h = 0.76 and 0.38, respectively; Table S1) (*11, 13*) and some exhibit multi-scaling (i.e., curved data clouds), complicating interpretation (*13*). These seminal efforts, and their discrepancies, motivate our global field-scale analysis to determine whether the previously reported variability in A-to-L relationships is representative of a larger, more diverse set of field

deltas, or whether a unified relationship analogous to Hack's law also emerges at the field scale. Specifically, we analyzed a comprehensive global dataset of 30 distributary networks spanning a range of scales and hydrodynamics (Fig. 1b; Table S2) (*30, 31*). Below, we show that our analysis has revealed unexpected insights into the deltaic land–building patterns driven by their distributary networks.

Hack's law in distributary channel networks of global river deltas

A fundamental challenge in quantifying delta land-building processes globally is the difficulty of systematically identifying nourishment areas. Here, we addressed this gap by leveraging an existing graph-theory framework to consistently delineate 5,892 nourishment areas across 30 distributary networks, enabling the first large-scale test of the scaling relationship between nourishment area (A) and the longest associated distributary channel length (L) among real-world deltas (Fig. 1b) (*30, 31*). In this framework, each distributary network is represented as a directed acyclic graph (*3*), where nodes correspond to bifurcations, confluences, and outlets, and edges represent channels with assigned water and sediment flow directions, based on delta gradient and limited field measurements (Fig. 1c) (*31,32*). This graph-based approach enabled us to systematically define the nourishment network for each bifurcation, referred to as the nourishment apex (*14*), which comprises all downstream nodes and channels. The longest channel path from the nourishment apex to the coast was then extracted and measured (see details in the supplementary material, Fig. 1c, fig. S1), and the nourishment area was estimated by summing the areas of the channel and interchannel regions within the nourishment network. To constrain uncertainty, we calculated three nourishment areas based on three local channel width buffers (b): 0×, 1×, 2×b (Fig. 1d), and used the mean value for our subsequent analyses (fig. S1) (*32,33*). This approach accounts for observed floodplain advection limits of bed material, such as fine to medium sand and flocculated mud (grain size ~ 62.5–350 μm) (*33,34*), which are the building blocks of deltaic land (Fig. 1d) (*33–35*). The perimeter of the nourishment area at the coast was defined using previously mapped subaerial shorelines (Fig. 1c) (*30, 31*). Although the graph-theory approach enabled us to map numerous A- and L-pairs consistently, it assumes unidirectional flow and therefore does not explicitly examine the bidirectional flow paths and sedimentation due to waves and tides (*14*). Nevertheless, the observed channel and nourishment area morphology reflects these marine influences, so they are implicitly incorporated into our analyses and may introduce variability (*14, 30*). Additionally, although subaqueous delta channel networks are known to be part of deltaic progradation (*36*), they remain difficult to measure without detailed bathymetric data. For the scope of this work, we focus on the subaerial delta, which is both more readily mapped and more societally relevant. Given the above mapping and uncertainty-constraining techniques, the nourishment areas measured herein represent a conservative geometric estimate of subaerial deltaic land area nourished by riverine bed material on a decadal timescale (*4, 12, 15, 19, 35*).

We found a global power law relationship as follows (Fig. 2a):

$$L = 1.43 \pm^{0.22}_{0.19} A^{0.60 \pm 0.018} \quad (1).$$

The exponent and coefficient (± 95% confidence intervals) of this global relation are remarkably similar to Hack's law (*20*): $L_t = 1.4A_t^{0.6}$. We also explored a normalized relationship between A and L to compare across delta size, such that A was normalized to the delta area and L was normalized by the main channel width (B), i.e., the river's width measured upstream of the first bifurcation near the delta apex (Fig. 2b) (*11*). Still, the resultant scaling exponent for this robust

(R^2 = 0.95) dimensionless relation (h = 0.6±0.020) remains the same as the dimensional form, indicating that delta nourishment areas follow a constant length-to-area scaling across nearly six orders of magnitude of delta sizes (Fig. 2b). From a land-building perspective, delta nourishment areas globally are elongated (h > 0.5), suggesting a preferential downstream growth direction towards the receiving basins. Additionally, a detailed sensitivity analysis addressing the uncertainty in the nourishment area and channel length measurements demonstrates that our results remain consistent despite these uncertainties (see supplementary materials; Table S3).

Apparent global Hack's law conceals two land–building patterns at the local scale

Although statistically rigorous, the dimensionless power-law relation exhibits considerable variability, suggesting the presence of additional geometric relationships. We thus further examined the origin of such variability within individual deltas. Surprisingly, we found two distinct delta land-building patterns among our 29 studied deltas (the Wairau Delta was excluded from the subanalysis due to limited measurements). One group, denoted as the Uniform Delta Network, conforms well to the global scaling law and Hack's law of tributary networks (h ~ 0.6) across all nourishment area sizes (h = 0.66±0.14; 14 out of 29 deltas; Figs. 3a, c, figs. S2, S3). For the second group of deltas (15 out of 29 deltas, Figs. 3b, d, figs. S4, S5), denoted as the Composite Delta Network, we observed a scale break. In other words, nourishment areas in Composite Delta Networks do not have a single scaling factor (i.e., a single value of h), but instead have two different scaling exponents within a single individual delta network. The scaling exponent for nourishment areas downstream of the scale break, i.e., near the shoreline, is close to linear ($L \sim A^1$), with h_1 = 0.83 ± 0.13. In contrast, upstream of the break, near the delta apex, the exponent is closer to the square root ($L \sim A^{0.5}$), h_2 = 0.53±0.28 (Fig. 4a). Interestingly, the scaling relation derived from aggregating measurements from several Composite Deltas of different sizes conforms to Hack's law and is similar to the relationships observed in individual Uniform Delta Networks, suggesting that Composite Networks are masked within the global trend, giving rise to the appearance of a universal scaling law (Fig. 3e). Still, the average is h = 0.60 ± 0.043 (Fig. 3e).

In the absence of a robust process-based explanation, we propose possible geometric reasons for the distinction between Uniform and Composite Delta Networks. River deltas with Uniform Networks are often confined in valleys (8 out of 14 Uniform Delta Networks, 57%, data S1) (*37*). Recall that Hack's law in tributary networks arises mainly due to a clear preferential flow direction from the tributary channels near the drainage divide to the basin outlet, following the basin's topographic gradient (slope). Moreover, based on fractal and optimal network theories (*21, 22, 26*), the networks with a preferred flow direction, like directed random walk/percolation (*21, 22, 26*), will be optimized to have more down-valley flowing channels compared to transverse flowing channels to maximize drainage efficiency (*26*), so that the drainage basin is elongated (h > 0.5). We hypothesize that the above rationale is analogous to Uniform Delta Networks, whereby the valley confinement sets a preferential flow direction from the delta apex to the valley exit near the coast, similar to topographic gradient in a drainage basin (*22*). The channel path that receives more flow undergoes greater erosion (*36*) and maintains this advantage as channels compete for discharge (*16*), thereby maximizing distributary efficiency for the distributary networks to grow toward the receiving basin (h ~ 0.6), similar to what is observed for tributary networks. While the preferential down-valley path is prone to channel avulsion, the avulsed new path and subsequent development of a new distributary network would still be affected by the same constraint (valley confinement), contributing to elongated growth.

Composite Delta Networks, in contrast, are often unconfined (12 out of 15 Composite Delta Networks, 80%, data S1), and the channel networks have freedom to build across a broader range of flow directions and paths. Without confinement, delta channels, on average, grow radially towards the receiving basins and freely fill the space of the broad deltaic plain without major spatial restrictions, resulting in an overall fan shape. With sufficient sediment supply and hydrodynamics relative to the size of interchannel area (*4, 11, 15, 16, 19*), the nourishment area A should follow $L \sim A^{0.5}$, indicating a free space-filling process (*22*) ($h \sim 0.5$), consistent with our observations of the upstream portion of Composite Delta Networks ($h_2 = 0.53 \pm 0.28$).

As deltas prograde, distributary channels repeatedly bifurcate due to mouth-bar deposition, which promotes splitting (*16, 38, 39*). With each bifurcation, water discharge is partitioned, and subordinate channels narrow (*16, 32, 40*), as the transverse sediment-spreading width between channel banklines and island edges (i.e., the nearest-edge distance), which represents the advection limit of overbank sediment, scales with channel width (*11, 15*). Thus, the total sediment-spreading region of the narrowing channels cannot keep pace with the rapidly growing delta perimeter (i.e., the radially averaged subaerial shoreline) as the delta progrades. The growing gap between channels, coupled with preferential coarse-grained sedimentation near channel banklines (*12, 15, 36*), produces elongated strips of subaerial land. The resulting nourishment zones are elongated, driving h toward unity (*36*, *41*), consistent with our measurements in downstream Composite Delta Networks ($h_1 = 0.83 \pm 0.13$).

These proposed geometric explanations are consistent with measurements of channel outlet spacing, which is expected to be more closely spaced in Composite Delta Networks because of linearly protruding growth near the coastline. The Euclidean (exact, straight-line) distance between outlets was measured for each delta network and normalized by the sum of such distances to calculate the normalized outlet spacing (L_o, see supplementary material). This metric, L_o, shows that outlets are 3 times more closely spaced for Composite Delta Networks compared to Uniform Delta Networks, with $L_o = 0.06 \pm 0.03$ and 0.18 ± 0.13, respectively (Fig. 4b). These results further support the distinctions between the two network patterns, which have unique characteristics of channel encroachment at the shoreline.

However, there are cases of Uniform Delta Networks that can emerge from unconfined deltas (6 out of 14 Uniform Delta Networks, 43%, data S1). We hypothesize that this may be due to mechanisms that inhibit the downstream protruding growth of the channel network and deltaic land building beyond the scale break, preventing the development of a Composite Delta Network. For example, deltas with intense wave climates (4 out of 6 unconfined Uniform Delta Networks) often have only a few main branches because longshore wave current drives sediment transport to smooth the irregular deltaic shoreline and close river mouths (*42*), thereby constraining network growth even in unconfined deltas (*2*). Thus, we hypothesize that the quasi-linear growth region of the Composite Delta Network is hindered under wave-influenced conditions, thereby eliminating the scale break and making the network appear uniform. A similar conceptual model of confinement has also been proposed to explain A and L relations derived from numerically simulated deltas (*13*) (Fig. 4A). In that model, the opening angle acts as a proxy for confinement, with a larger opening angle indicating less confinement, resulting in $L \sim A^{0.5}$ (*13*). Conversely, a smaller opening angle indicates more confined land growth, leading to relations closer to $L \sim A^1$ (*13*). In addition to marine influences, juvenile deltas may not yet have grown to a size where a scale break can occur (2 out of 6 unconfined Uniform Delta Networks), including Wax Lake (*12, 19, 36*) and the Mississippi River (most seaward region, known as the “bird's foot” or the La Balize

lobe) deltas (*43*). These two deltas are about 0.05 and 0.5–1 ka in age, respectively (*12, 43*), relative to the Holocene-aged (~7−10 ka) Composite Network Selenga Delta (*32, 40*).

The above geometric rationale also explains the spatial variation in the location of the scale break across different delta hydrodynamics. This break occurs around (33±24)×B for most river-dominated deltas, where scale breaks are measured as distance from the shoreline and normalized by B. River-dominated deltas typically form dendritic distributary networks, with bifurcations increasing downstream as mouth bars develop (*38, 39*). Mouth bar-controlled distributaries have a characteristic length of ~10×main channel width (B), based on theory and observation (*38, 39*). Because the transverse sediment spreading width remains ~ 2×local channel width (b) (*11*), each narrowing channel toward the coast produces a smaller nourishment area, consistent with $L \sim A^1$ (*36, 41*) (Fig. 4c). In larger deltas, however, where channel length exceeds ~10×B, other processes such as avulsion and tidal influence dominate. Notably, avulsion length scales with the backwater length, which can exceed 100×B (*17, 18, 39*). Similarly, the scale break shifts more inland to (78±46)×B for river deltas with a strong tidal influence. We hypothesize this reflects tidal hydrodynamics that keep channels open by transporting sediment landward along the valley axis ($h \sim 1$). As tidal forcing decreases landward, typically ~(10–100)×B from the coastline (*44*) (Fig. 4c), the riverine forcing (e.g., river floods) regains control and develops the transverse, cross valley portion of the network, following the square-root scaling factor ($h \sim 0.5$).

In both Uniform and Composite Delta Networks, a few exceptional cases exhibit superlinear scaling relations ($h > 1$) (Fig. 4a), where the channel length grows faster, per unit, than the nourishment area. This can arise under valley confinement, as in the Paraná delta, where a confined braided delta plain restricts area while braiding increases channel length ($h = 1.46 \pm 0.02$; Fig. S5). Similarly, in tide-dominated systems such as the Coville and Red deltas, tidal forcing promotes sinuosity and looping (*44, 45*), causing distributary length to outpace area growth, again yielding $h > 1$ (figs. S4, S5).

Implications of Hack's law in river deltas

By analyzing extensive real-world data, we confirmed a consistent power-law relation between nourishment area A and the longest channel length L in river deltas, analogous to Hack's law in tributary networks, as previously hypothesized (*11*, *13*) (Fig. 4a). This global relation can serve as a rule of thumb for estimating deltaic land-building when specific boundary conditions, such as diverse hydrodynamic influences (e.g., waves, tides), sediment type, and confinement, are unknown (*11*). Moreover, this framework can also inform restoration efforts and paleoenvironmental assessments. For example, by targeting interchannel areas within quasi-linear-scaling nourishment zones, the delta can transition more quickly into space-filling regimes. Also, given that delta size correlates with water and sediment supply (*1–4*, *18*), such scaling relationships, when paired with channel length and nourishment area measurements from paleo-delta deposits on Earth and Mars (46), could also be used to infer discharges, offering a novel tool for reconstructing past climates. Furthermore, this relation can also benchmark numerical and experimental deltas (*11*, *13*). However, this global simplicity may conceal local variability, such as scaling breaks, which warrant caution when applying global findings to local contexts.

Despite the global A–L scaling, ~50% of deltas show local variability marked by a scale break (Composite Delta Networks). In the absence of a process-based explanation, we propose a straightforward geometric rationale (Fig. 4d): because river deltas maintain roughly stable

dimensionless transverse sediment spreading width between channels and islands (i.e. nearest edge distance; *11*), due to similar advection length of over-bank sediment (*11, 15*), wide trunk channels could entirely occupy space upstream, where shoreline and interchannel spacing are small. In contrast, downstream, the sediment spreading width of narrowing channels cannot keep pace with the expanding interchannel areas, leading to quasi-linear growth. This process does not apply to Uniform Delta Networks, as the preferential flow direction will reshape the interchange island from the apex.

Scale breaks have also been observed in tributary networks, where scaling shifts reflect geologic controls. For example, h transitions from ~0.62–0.67in regional basins to 0.5–1 in continental basins, and from advective channels ($h \sim 0.6$) to hillslope heads dominated by diffusion ($h \sim 1$) (*22*). By contrast, the channel tips of deltas are mostly subaqueous, limiting the availability of large datasets (*36*). Because our work focuses only on the subaerial delta, whether additional scale break(s) occur between subaerial and subaqueous delta networks remains unresolved and is an exciting avenue for future work. Furthermore, valley confinement plays a vital role in determining the complexity of the delta network, as others have shown, including hypsometry and delta slope (*47*). However, a physical understanding of how confinement impacts river delta morphology remains lacking, which could lead to a process-based reasoning for the scale breaks. In addition, past work has shown that the nearest edge distance can vary in a delta (*48*), possibly due to tidal influences (*11*, *48*), which could help explain the location of scale breaks.

Our results raise the broader question of why river networks, from uppermost tributaries to the lowermost distributaries, share the same Hack's law? (*11, 13, 22*, *49*) We may draw exciting parallels between the two fields, which reveal universality within river network studies and help understand their common physics. For instance, we may ask questions like where a delta channel truly begins (or ends), paralleling long-standing debates over channel heads in tributary systems (*50*). Future studies may also investigate whether additional delta network metrics, such as slope–area scaling, widely used in tributary systems, yield new insights into distributary organization.

References and Notes

1. J.H. Nienhuis, W. Kim, G.A. Milne, M. Quock, A.B. Slangen, T.E. Törnqvist, River deltas and sea-level rise. *Annual Review of Earth and Planetary Sciences*, **51**, 79-104 (2023). doi.org/10.1146/annurev-earth-031621-093732.
2. J.H. Nienhuis, A.D. Ashton, D.A. Edmonds, A.J.F. Hoitink, A.J. Kettner, J.C. Rowland, T.E. Törnqvist, Global-scale human impact on delta morphology has led to net land area gain. *Nature*, **577**, 514-518 (2020). doi.org/10.1038/s41586-019-1905-9.
3. A.J. Hoitink, J.A. Nittrouer, P. Passalacqua, J.B. Shaw, E.J. Langendoen, Y. Huismans, D.S. van Maren, Resilience of river deltas in the Anthropocene. *Journal of Geophysical Research: Earth Surface*, **125**, e2019JF005201 (2020). doi.org/10.1029/2019JF005201.
4. D.A. Edmonds, S.C. Toby, C.G. Siverd, R. Twilley, S.J. Bentley, S. Hagen, K. Xu, Land loss due to human-altered sediment budget in the Mississippi River Delta. *Nature Sustainability*, **6**, 644-651 (2023).
5. D.A. Edmonds, R.L. Caldwell, E.S. Brondizio, S.M. Siani, Coastal flooding will disproportionately impact people on river deltas. *Nature Communications*, **11**, 4741 (2020). doi.org/10.1038/s41893-023-01081-0.

6. K.M. Sanks, J.B. Shaw, K. Naithani, Field-based estimate of the sediment deficit in coastal Louisiana. *Journal of Geophysical Research: Earth Surface*, **125**, e2019JF005389 (2020). doi.org/10.1029/2019JF005389.

7. J.P.M. Syvitski, C.J. Vörösmarty, A.J. Kettner, P. Green, Impact of Humans on the Flux of Terrestrial Sediment to the Global Coastal Ocean. *Science*, **308**, 376–380 (2005). doi.org/10.1126/science.1109454.

8. S.H. Ensign, J.N. Halls, E.K. Peck, Watershed sediment cannot offset sea level rise in most US tidal wetlands. *Science*, **382**, 1191–1195 (2023). doi.org/10.1126/science.adj0513.

9. P. Passalacqua, The Delta Connectome: A network-based framework for studying connectivity in river deltas. *Geomorphology*, **277**, 50-62 (2017). doi.org/10.1016/j.geomorph.2016.04.001.

10. A. Tejedor, A. Longjas, D.A. Edmonds, I. Zaliapin, T.T. Georgiou, A. Rinaldo, E. Foufoula-Georgiou, Entropy and optimality in river deltas. *Proceedings of the National Academy of Sciences*, **114**, 11651-11656 (2017). doi.org/10.1073/pnas.1708404114.

11. D.A. Edmonds, C. Paola, D.C. Hoyal, B.A. Sheets, Quantitative metrics that describe river deltas and their channel networks. *Journal of Geophysical Research: Earth Surface*, **116**, (2011). doi.org/10.1029/2010JF001955.

12. J.B. Shaw, D. Mohrig, R.W. Wagner, Flow patterns and morphology of a prograding river delta. *Journal of Geophysical Research: Earth Surface*, **121**, 372-391 (2016). doi.org/10.1002/2015JF003570.

13. M. Liang, C. Van Dyk, P. Passalacqua, Quantifying the patterns and dynamics of river deltas under conditions of steady forcing and relative sea level rise. Journal of Geophysical Research: Earth Surface, **121**, 465-496 (2016). doi.org/10.1002/2015JF003653.

14. A. Tejedor, A. Longjas, I. Zaliapin, E. Foufoula-Georgiou, Delta channel networks: 1. A graph-theoretic approach for studying connectivity and steady state transport on deltaic surfaces. *Water Resources Research*, **51**, 3998-4018 (2015). doi.org/10.1002/2014WR016577.

15. G. Salter, M.P. Lamb, Autocyclic secondary channels stabilize deltaic islands undergoing relative sea level rise. *Geophysical Research Letters*, **49**, e2022GL098885 (2022). doi.org/10.1029/2022GL098885.

16. M.G. Kleinhans, R.I. Ferguson, S.N. Lane, R.J. Hardy, Splitting rivers at their seams: bifurcations and avulsion. *Earth surface processes and landforms*, **38**, 47-61 (2013). doi.org/10.1002/esp.3268.

17. S. Brooke, A.J. Chadwick, J. Silvestre, M.P. Lamb, D.A. Edmonds, V. Ganti, Where rivers jump course. *Science*, **376**, 987-990 (2022). doi.org/10.1126/science.abm1215

18. V. Ganti, A.J. Chadwick, H.J. Hassenruck-Gudipati, B.M. Fuller, M.P. Lamb, Experimental river delta size set by multiple floods and backwater hydrodynamics. *Sci Adv 2*, e1501768 (2016). doi.org/10.1126/sciadv.1501768.

19. K. Wright, J. Hariharan, P. Passalacqua, G. Salter, M.P. Lamb, From grains to plastics: Modeling nourishment patterns and hydraulic sorting of fluvially transported materials in deltas. *Journal of Geophysical Research: Earth Surface*, **127**, e2022JF006769 (2022). doi.org/10.1029/2022JF006769.

20. J.T. Hack, Studies of longitudinal stream profiles in Virginia and Maryland. *US Government Printing Office*, **294** (1957). doi.org/10.3133/pp294B.

21. R. Rigon, I. Rodriguez-Iturbe, A. Maritan, A. Giacometti, D.G. Tarboton, A. Rinaldo, On Hack's law. *Water Resources Research*, **32**, 3367-3374 (1996). doi.org/10.1029/96WR02397.

22. P.S. Dodds, D.H. Rothman, Scaling, universality, and geomorphology. *Annual Review of Earth and Planetary Sciences*, **28**, 571-610 (2000). doi.org/10.1146/annurev.earth.28.1.571.

23. T. Sassolas-Serrayet, R. Cattin, M. Ferry, The shape of watersheds. *Nature Communications*, **9**, 3791 (2018). doi.org/10.1038/s41467-018-06210-4.

24. R.S. Yi, Á. Arredondo, E. Stansifer, H. Seybold, D.H. Rothman, Shapes of river networks. *Proceedings of the Royal Society A: Mathematical, Physical and Engineering Sciences*, **474**, 20180081 (2018). doi.org/10.1098/rspa.2018.0081.

25. W. Luo, A.D. Howard, R.A. Craddock, E.A. Oliveira, R.S. Pires, The global spatial distribution of Hack's law exponent on Mars is consistent with an Early arid climate. *Geophysical Research Letters*, **50**, e2022GL102604 (2023). doi.org/10.1029/2022GL102604.

26. R. Rigon, A. Rinaldo, I. Rodriguez-Iturbe, R.L. Bras, E. Ijjasz-Vasquez, Optimal channel networks: a framework for the study of river basin morphology. *Water Resources Research*, **29**, 1635-1646 (1993). doi.org/10.1029/92WR02985.

27. J.T. Perron, P.W. Richardson, K.L. Ferrier, M. Lapôtre, The root of branching river networks. *Nature*, **492**, 100-103 (2012). doi.org/10.1038/nature11672.

28. Q. Li, N.M. Gasparini, K.M. Straub, Some signals are not the same as they appear: How do erosional landscapes transform tectonic history into sediment flux records? *Geology*, **46**, 407-410 (2018). doi.org/10.1130/G40026.1.

29. L. Vulis, A. Tejedor, H. Ma, J.H. Nienhuis, C. Broaddus, J. Brown, D.A. Edmonds, J.C. Rowland, E. Foufoula-Georgiou, River delta morphotypes emerge from multiscale characterization of shorelines. *Geophysical Research Letters*, **50**, e2022GL102684 (2023). doi.org/10.1029/2022GL102684.

30. J. Hariharan, A. Piliouras, J. Schwenk, P. Passalacqua, Width-based discharge partitioning in distributary networks: How right we are. *Geophysical Research Letters*, **49**, e2022GL097897 (2022). doi.org/10.1029/2022GL097897.

31. J. Schwenk, A. Piliouras, J.C. Rowland, Determining flow directions in river channel networks using planform morphology and topology. *Earth Surface Dynamics*, **8**, 87-102 (2020). doi.org/10.5194/esurf-8-87-2020.

32. T.Y. Dong, J.A. Nittrouer, B. McElroy, E. Il'icheva, M. Pavlov, H. Ma, A.J. Moodie, V.M. Moreido, Predicting water and sediment partitioning in a delta channel network under varying discharge conditions. *Water Resources Research*, **56**, e2020WR027199 (2020). doi.org/10.1029/2020WR027199.

33. J. Nghiem, G. Li, J. Harringmeyer, G. Salter, C. Fichot, K. Wright, P. Passalacqua, M. Lamb, Michael, Evidence for Mud as Flocculated Bed-Material Load Versus Washload in a River Delta. *Journal of Geophysical Research: Earth Surface*. **130**, e2025JF008366 (2025). doi.org/10.1029/2025JF008366.

34. M. Kim, B. Chun, E. Chamberlain, W. Kim, Enhanced mud retention as an autogenic mechanism for sustained delta growth: Insight from records of the Lafourche subdelta of the Mississippi River. *Sedimentology*, **72**, 165-188 (2025). doi.org/10.1111/sed.13230.

35. J.A. Nittrouer, J. Shaw, M.P. Lamb, D. Mohrig, Spatial and temporal trends for water-flow velocity and bed-material sediment transport in the lower Mississippi River. *Bulletin*, **124**, 400-414 (2012). doi.org/10.1130/B30497.1.

36. J.B. Shaw, D. Mohrig, The importance of erosion in distributary channel network growth, Wax Lake Delta, Louisiana, USA. *Geology*, **42**, 31-34 (2014). doi.org/10.1130/G34751.1.

37. O.A. Prasojo, T.B. Hoey, A. Owen, R.D. Williams, Slope break and avulsion locations scale consistently in global deltas. *Geophysical Research Letters*, **49**, e2021GL093656 (2022). doi.org/10.1029/2021GL093656.

38. D.A. Edmonds, R.L. Slingerland, Mechanics of river mouth bar formation: Implications for the morphodynamics of delta distributary networks. *Journal of Geophysical Research: Earth Surface*, **112** (2007). doi.org/10.1029/2006JF000574.

39. D.J. Jerolmack, J.B. Swenson, Scaling relationships and evolution of distributary networks on wave-influenced deltas. *Geophysical Research Letters*, **34**, (2007). doi.org/10.1029/2007GL031823.

40. T.Y. Dong, J.A. Nittrouer, E. Il'icheva, M. Pavlov, B. McElroy, M.J. Czapiga, H. Ma, G. Parker, Controls on gravel termination in seven distributary channels of the Selenga River Delta, Baikal Rift basin, Russia. *Geological Society of America Bulletin*, **128**, 1297-1312 (2016). doi.org/10.1130/B31427.1

41. W.T. Ke, J.B. Shaw, R.C. Mahon, C.A. Cathcart, Distributary channel networks as moving boundaries: Causes and morphodynamic effects. *Journal of Geophysical Research: Earth Surface*, **124**, 1878-1898 (2019). doi.org/10.1029/2019JF005084.

42. J.H. Nienhuis, A.D. Ashton, L. Giosan, What makes a delta wave-dominated? *Geology*, **43**, 511-514 (2015). doi.org/10.1130/G36518.1.

43. J.M. Coleman, H.H. Roberts, G.W. Stone, Mississippi River delta: an overview. *Journal of Coastal Research*, **14**, 699-716 (1998)

44. A.F. Hoitink, D.A. Jay, Tidal river dynamics: Implications for deltas. *Reviews of Geophysics*, **54**, 240-272 (2016). doi.org/10.1002/2015RG000507.

45. A. Konkol, J. Schwenk, E. Katifori, J.B. Shaw, Interplay of river and tidal forcings promotes loops in coastal channel networks. *Geophysical Research Letters*, **49**, e2022GL098284 (2022). doi.org/10.1029/2022GL098284.

46. R.A. DiBiase, A.B., Limaye, J.S. Scheingross, W.W. Fischer, M.P. Lamb, Deltaic deposits at Aeolis Dorsa: Sedimentary evidence for a standing body of water on the northern plains of Mars. *Journal of Geophysical Research: Planets*, **118**, 1285-1302 (2013). doi.org/10.1002/jgre.20100.

47. J.B. Shaw, K.M. Sanks, A. Piliouras, Basin confinement influences river delta elevation profiles. *Geological Society of America Bulletin,* (2025). doi.org/10.1130/B38386.1

48. P. Passalacqua, S. Lanzoni, C. Paola, A. Rinaldo, Geomorphic signatures of deltaic processes and vegetation: The Ganges-Brahmaputra-Jamuna case study, *Journal of Geophysical Research: Earth Surface*, **118**, 1838-1849 (2013). doi:10.1002/jgrf.20128.

49. J.M. Swartz, B.T. Cardenas, D. Mohrig, P. Passalacqua, Tributary channel networks formed by depositional processes. *Nature Geoscience*, **15**, 216-221 (2022). doi.org/10.1038/s41561-022-00900-x.

50. D.R. Montgomery, W.E. Dietrich, Where do channels begin? *Nature*, **336**, 232-234 (1988). doi.org/10.1038/336232a0.

51. T.Y. Dong, J.A. Nittrouer, M.J. Czapiga, H. Ma, B. McElroy, E. Il'icheva, M. Pavlov, S. Chalov, G. Parker, Roles of bank material in setting bankfull hydraulic geometry as informed by the Selenga River Delta, Russia. *Water Resources Research*, **55**, 827-846 (2019). doi.org/10.1029/2017WR021985.

52. E. Barefoot, T.M. Pavelsky, G.H. Allen, M.A. Zimmer, B.L. McGlynn, Temporally variable stream width and surface area distributions in a headwater catchment. *Water Resources Research*, **55**, 7166-7181 (2019). doi.org/10.1029/2018WR023877.

53. V.M. Muggeo, Segmented: an R package to fit regression models with broken-line relationships. *R news*. **8**, 20-25 (2008). Doi.org/10.32614/CRAN.package.segmented.

54. C. Pilgrim, Piecewise-regression (aka segmented regression) in Python. *Journal of Open Source Software*. **6,** (2021). doi.org/10.21105/joss.03859

55. T. Dong, L. Vulis, H. Ma, A. Tejedorand T. Goudge, Apparent Hack's Law in River Deltas. *Zenodo*. doi.org/10.5281/zenodo.17029586.

Acknowledgments: We thank the Earth Surface Processes Institute, run by the Community Surface Dynamics Modeling System (CSDMS), for connecting TYD and LV to conceptualize this work. We are grateful to senior editor Angela Hessler, Paola Passalacqua, and two anonymous reviewers for their insightful comments, which significantly improved the quality of this manuscript. TYD dedicates this work to the bright memory of CQ.

Funding:

National Science Foundation Division of Earth Sciences Postdoctoral Fellowship 1952814 (TD)

The University of California Lab Fees in Residence Graduate Fellowship Grant L21GF3569 (LV)

National Aeronautics and Space Administration Earth and Space Science Fellowship Grant 338-80NSSC18K1409 (LV)

National Science Foundation Division of Earth Sciences Grant 2342937 (AT)

National Science Foundation Division of Research, Innovation, Synergies and Education Grant 2425748 (AT)

Ministerio de Ciencia, Innovación y Universidades, Agencia Española de Investigación Grant PID2023-149409NB-I00 (AT)

Author contributions:

Conceptualization: TYD, LV, HM

Methodology: TYD, LV, AT

Investigation: TYD, LV, HM

Visualization: TYD

Funding acquisition: TYD, LV, HM, AT, TAG

Project administration: TYD

Supervision: TYD, HM, TAG

Writing – original draft: TYD

Writing – review & editing: TYD, LV, HM, AT, TAG

Competing interests: The Authors declare that they have no competing interests.

Data and materials availability: All data analyzed in this study are tabulated in the supplementary materials, and the associated Python codes are archived at 10.5281/zenodo.17029586 (*55*). The satellite imagery shown here is publicly available, namely, U.S. Geological Survey (USGS)/National Aeronautics and Space Administration Landsat satellite imagery, which is downloaded from the USGS Earth Explorer (https://earthexplorer.usgs.gov/). DCNs and shorelines used in this study are available via References (*30, 31*). This study did not generate new samples or physical materials.

Supplementary Materials

Materials and Methods

Figs. S1 to S34

Table S1 to S3

References (*51-54*)

Data S1 to S3

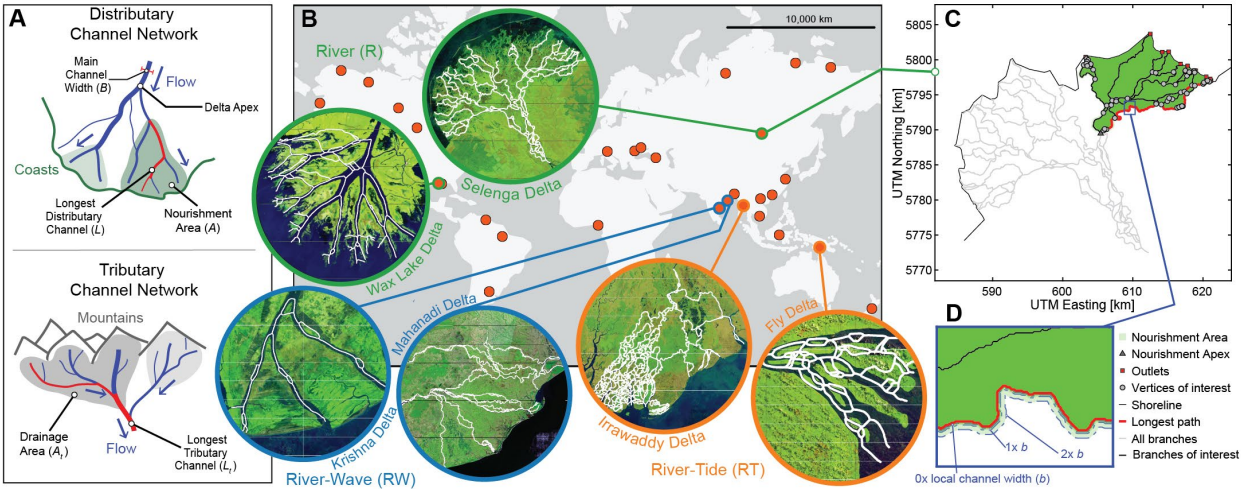

Fig. 1. Global river delta networks and nourishment areas. (**A**) Conceptual models illustrate the similarity between distributary deltas and tributary rivers in terms of channel networks. Here, B is the main channel width, measured upstream of the first bifurcation near the delta apex. L is the longest distributary channel, and A is the nourishment area. Similarly, L_t is the longest tributary channel, and A_t is the drainage area. (**B**) The data set of deltas (*30, 31*) used in this study covers a range of hydrodynamics, sizes, geography, valley confinement, and climate (*37, 47*). (**C**) The delineation of the nourishment area and the longest distributary channel are shown in the example of the Selenga River Delta (*32, 40, 50*). (**D**) Detailed view of the uncertainty range for the perimeter of the nourishment area. Here, b is the local channel width used to buffer the perimeter from 0 to 2x b, accounting for measurement uncertainties in the area and length of distributaries; see details in the main text and supplementary materials.

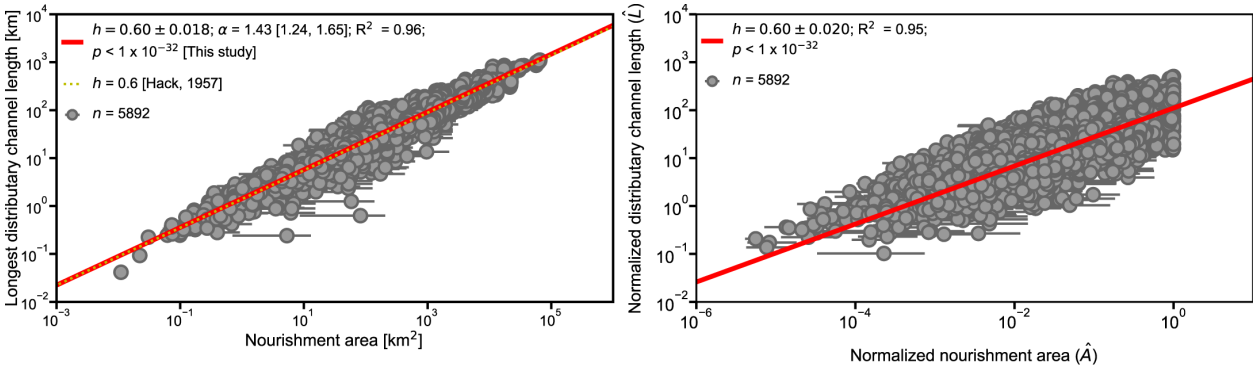

Fig. 2. The scaling between distributary channel length and nourishment area in global river deltas. (**A**) Dimensional and (**B**) dimensionless (*11*) scaling law of the distributary channel network of nourishment area (A) and the length (L) of the longest distributary channel in that area, obtained from 5,982 measurements across 30 deltas. Parameter n is the number of data points used for the regression. R^2 and p-values are reported. Error bars represent the range of A, among 0×, 1×, and 2× local channel width (b), as shown in the buffer area boundary. Hack's law is shown in panel A as a yellow dotted line for comparison.

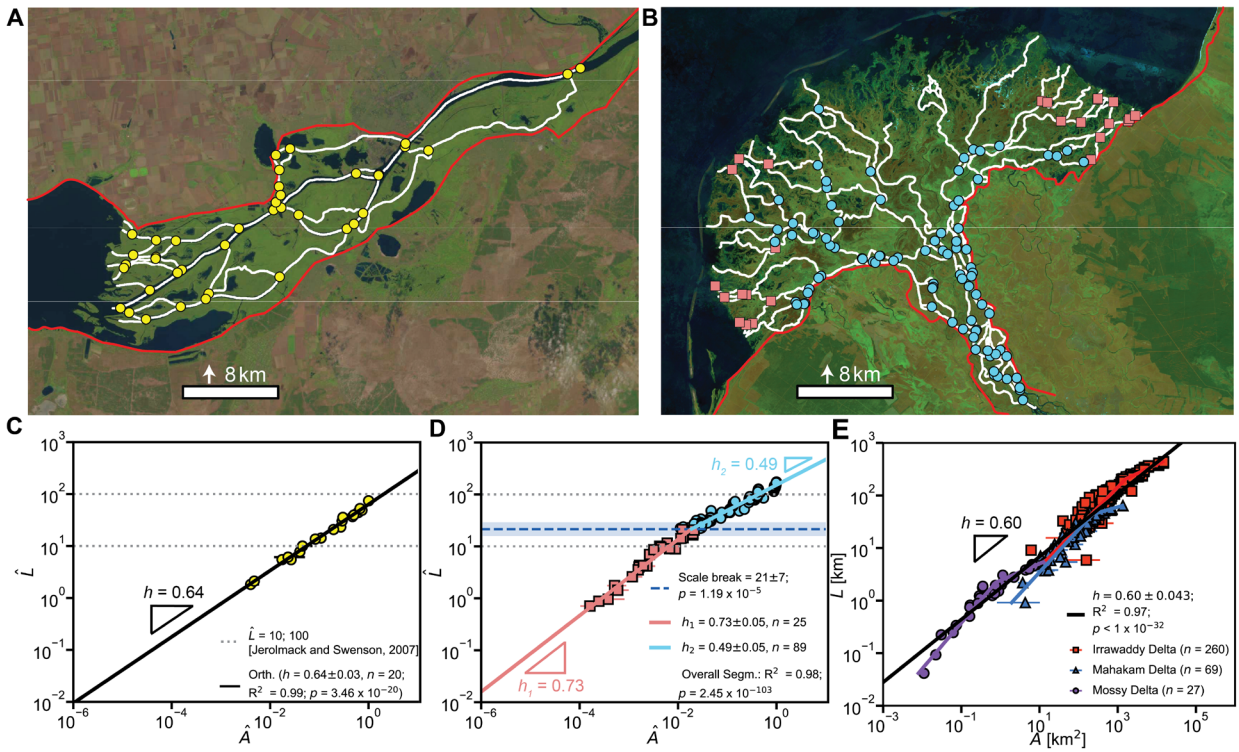

Fig. 1. Distinct deltaic land-building patterns for Uniform and Composite Delta Networks. Examples of Uniform (**A**) and Composite (**B**) Delta Networks: the Dnieper and Selenga Deltas, respectively. Maps show the planform distribution of nourishment apexes (circles and squares) for each scaling regime. Red outlines indicate the extent of valley confinement (*37, 47*), whereas white lines highlight the distributary channel network. (**C**) and (**D**) show the corresponding scaling law of the normalized nourishment area ($\widehat{A}$) versus the length of the longest distributary channel ($\widehat{L}$), respectively, where the nourishment area is normalized by the delta area, and the channel width of the main branch normalizes the distributary channel length. Note that the scale break occurs at distances that are multiples of the channel width, separating the quasi-linear and square-root scaling regimes. (**E**) Dimensional scaling relations between channel length (L) and nourishment area (A) obtained by aggregating multiple Composite Delta Networks of different sizes conform to Hack's law and are similar to those from individual Uniform Delta Networks. R^2 and p-values are reported. Parameter n is the number of data points used in the regressions. Error bars represent the range of A, among 0×, 1×, and 2× local channel width (b), as shown in the buffer area boundary.

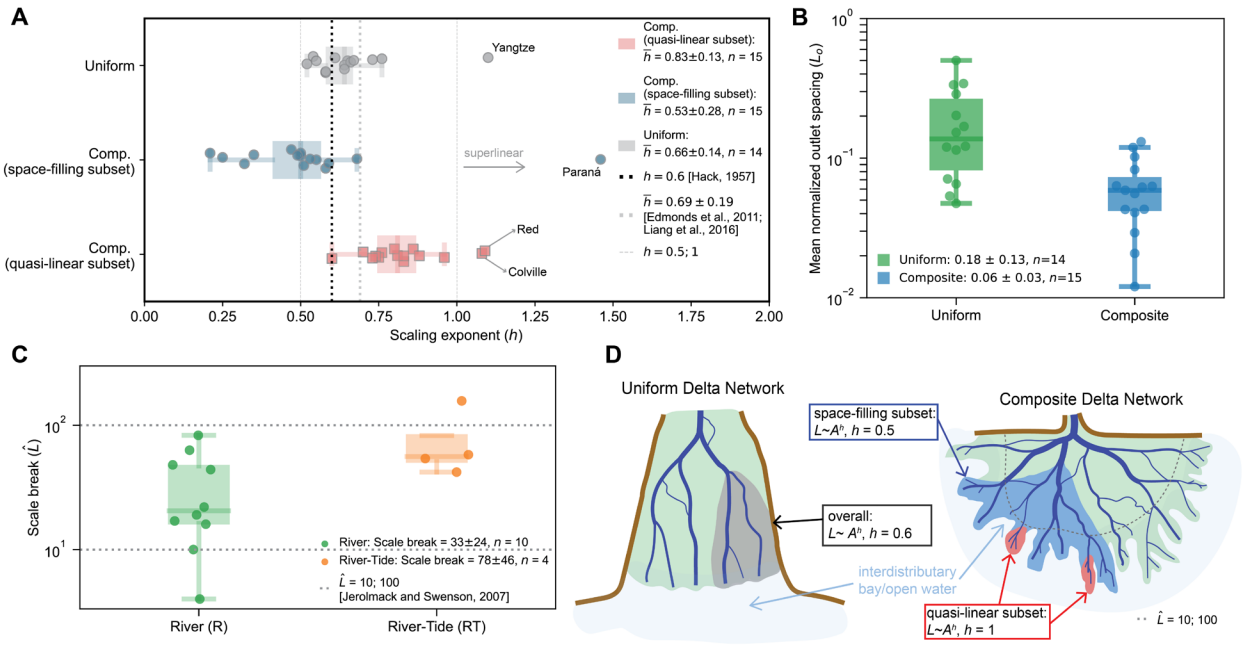

Fig. 4. Hydrodynamic conditions and distinct shoreline morphology for Uniform and Composite Delta Networks. (**A**) Scaling exponent *h* for the entire data set for different channel network patterns. *n* is the number of data points. (**B**) Mean normalized outlet spacing (L_o) for river deltas with Uniform and Composite Network patterns. (**C**) Locations of the scale break across hydrodynamics as a function of normalized channel length ($\widehat{L}$). (**D**) Conceptual model summarizing the scaling law in river deltas with uniform and composite network patterns. Boxes in panels B and C indicate interquartile range (IQR, 75% - 25%), and lines inside the boxes are the medians. Whiskers and caps represent ±1.5× IQR.

Science
AAAS

Supplementary Materials for

Apparent Hack's Law in River Deltas

Tian Y. Dong, Lawrence Vulis, Hongbo Ma, Alejandro Tejedor, Timothy A. Goudge

Corresponding author: tian.dong@utrgv.edu, hongboma@illinois.edu

The PDF file includes:

Materials and Methods
Figs. S1 to S34
Tables S1 to S3

Other Supplementary Materials for this manuscript include the following:

Data S1 to S3
Archived codes: doi.org/10.5281/zenodo.17029586

Materials and Methods

Defining the Delta Nourishment Network and Area and the Longest Distributary Channel

Thirty delta channel networks, spanning a range of scales, hydrodynamics, valley confinement (*30, 31, 37, 47*), and climates, are used for analysis in this paper and were compiled from previous work (Fig. 1b, Table S1) (*30, 31, 37, 47*). Each distributary network is abstracted as a directed acyclic graph (G), where $G = \{V, E\}$, with V (also denoted as nodes) representing bifurcations, confluences, and outlets, and E (also denoted as links) representing the channels (*14*). Edge directionality is assigned according to the flow direction (i.e., water and sediment discharges in the channels), estimated using the graph model, and based on a suite of direction-predicting algorithms using inputs like the regional delta gradient and characteristics of the delta network, and is tested against limited field measurements (*30, 32*). Starting from the associated graph of each distributary network, the nourishment network is defined for each bifurcation (termed a nourishment apex, similar to the pour point in drainage basins) (*14*), consisting of all its downstream bifurcations, confluences, outlets, and channels. Previous studies extracted channel networks from their centerlines and provided this data in a geographic representation, i.e., shapefiles of the channel centerlines and individual bifurcations, and the associated network theoretic representation through a graph adjacency matrix (Fig. 1c). A nourishment network of channel centerlines (i.e., a channel network skeleton) is defined for each nourishment apex, which contains all the downstream links and vertices fed by that node (*11, 14, 19, 30–32*). Confluence nodes and networks with only one outlet are excluded from the analysis. Predicted water discharge from these graphs was well tested against field measurements, further supporting the accuracy of the connectivity of the distributary network (*30, 31*).

After defining a nourishment network, the nourishment area is determined by filling the space between the distributary channels (i.e., links). First, channel width polygons are created by buffering each link with its average width (Fig. 1c). The channel polygons are then merged and filled to include areas of interdistributary islands between the channels, using the Python package Shapely, to create nourishment area polygons for each nourishment apex. True nourishment areas (i.e., downstream areas a particle may reach once it passes a bifurcation) can vary for materials with specific gravities (*19*), e.g., sand versus organic particles (*19*). Limited observations and theories (*11, 15, 34*) suggest that the space between the bank and the island edge is relatively stable along channels, possibly due to the relatively stable sediment advection length of suspended sediment. Therefore, we use a straightforward assumption by buffering the nourishment area perimeter with a length that scales with multiples of the local channel width ($0\times$, $1\times$, $2\times b$; Fig. 1d, fig. S1), accounting for the field-observed transport limit of bed material, including fine to medium sand and flocculated mud (grain size of ~62.5–350 μm) (*33, 35*). Depending on the flow condition, bed material sand can be transported as suspended and bed load (*33, 35*), such that these grain sizes can nourish the distributary network and the surrounding broad interchannel areas, like the island interiors (*35*). Finally, previous work manually mapped subaerial shorelines using mean water masks to delineate the perimeter of the nourishment area along the coast (Fig. 1d) (*30, 31*). In prior work (*30, 31*), deltaic shorelines and networks are sometimes extracted from a single image at a time to validate flow magnitude and direction, which could introduce additional uncertainty in channel-length measurements, as constrained by the sensitivity analysis detailed below. While there may be changes in small parts of the network from image to image, the overall connectivity structures, such as primary channels, are preserved and remain unchanged in the

deltas in our dataset over multiple decades (*10, 14*). Thus, given the above mapping and uncertainty-constraining techniques, the nourishment areas measured herein represent a conservative geometric estimate of subaerial deltaic land area nourished by bed material sand on a decadal timescale (*4, 12, 19, 32*). Finally, the mean and range of nourishment areas are reported and used for analysis in this study. One limitation of this buffer approach is that gaps can appear between two sub-nourishment areas. However, these gaps are still included by the larger, upstream nourishment areas. Importantly, all deltaic land belongs to at least one nourishment area, so no subaerial land is omitted from our analyses. The sensitivity of this buffer approach is tested in a section below.

The length and flow direction of the channel centerline, as determined from previous work, are included for each nourishment area (*30, 31*). Based on the flow direction and number of nodes (N), a weighted adjacency matrix, N x N, of channel length is created for each nourishment area, following previous work (*14*). After assigning a negative sign to the adjacency matrix, the longest path from the nourishment apex to an outlet becomes the shortest path problem, allowing for a trivial solution for Directed Acyclic Graphs and being easily solved via the MATLAB function shortest path (Fig. 1c) (*14*).

Linear Regressions of Length versus Area and Finding the Scale Break

Following previous works (*51*), a linear mixed-effect model, with an independent random effect on the intercept and coefficient, is used for the global dataset to derive the global scaling law, accounting for delta size and climate uncertainties. The relationship between the normalized longest channel length and nourishment area for the Uniform Delta Network is determined through orthogonal linear regression, which accounts for uncertainties in both area and length (*51*). For Composite Delta Networks, segmented regression via the Python package piecewise regression was used to verify the statistical significance and location of the scale breaks (*53, 54*). The Davies test evaluates the null hypothesis of no scale break (*53, 54*). Uncertainty ranges and p-values are reported for the location of the scale breaks, exponents, and coefficients of the scaling law for each delta (Figs. 2, 3, figs. S2–S5).

Sensitivity Analysis

Uncertainties remain in measuring the nourishment area and channel length due to reliance on previously published channel networks. Water masks used to extract channel networks are not always representative of average conditions, due to limited satellite coverage, which affects estimates of channel length (*30, 31*). Similarly, the boundaries between the nourishment areas in the low-relief deltas are challenging to identify (*12*). We used the overbank sediment transport advection length as a proxy, based on theory and observations that the space between channel bank and island edge scales with channel width; however, field measurements remain sparse, rendering sensitivity analyses necessary (*15, 33*).

To test the robustness of our results, we performed sensitivity analyses. First, we introduced uniformly distributed random errors (1–5%) to the channel length to account for water mask and shoreline mapping uncertainty. For each delta, we then constructed regressions linking nourishment area to error-adjusted channel length with three widths (b) buffers (0×, 1×, 2× b). Comparison with the main-text results showed only minor shifts in exponents (mean values for the buffers are h_1 = 0.76±0.13–0.91±0.22 and is main text is h_1 = 0.83±0.13; mean values for the

buffers are h_2 = 0.52±0.29–0.55±0.26 and in the main text is h_2 = 0.53±0.28), and scale breaks (mean values for the buffers range from 50±53 to 67±65 and in the main text is 62 ±60; figs. S6–S24). Two cases, Amazon and Coville, with 2× buffers, had high p-values, but removing them from the Composite Delta Network group did not alter the statistics. Likewise, excluding Coville, Red, and Paraná, which exhibit superlinear scaling ($h > 1$), also left the results unchanged (Table S3).

Due to the large size of Lena and Ganges-Brahmaputra-Jamuna deltas (GBJD), they account for 42% of the overall data points (2469 out of the overall 5892 nourishment areas mapped), an additional sensitivity analysis is conducted to assess the robustness of the scaling relationships derived from the global data with respect to this size bias. We perform the same regression analysis on three cases: 1) the subdataset without Lena Delta (4557 out of 5892 data points used), 2) the subdataset without GBJD (4758 out of 5892 data points used), and 3) the subdataset without both deltas (3432 out of 5892 data points used). Overall, the power-law relations between distributary channel length and nourishment areas from all three subset cases are not only consistent with respect to the main text but also remarkably similar to Hack's law (coefficient = 1.4, exponent = 0.6), with coefficients that range from 1.38 to 1.40, and exponents of 0.61 (figs. S27–29; Table S3). Also, looking at the impact of removing these two deltas on the overall statistics of the Hack's law exponent (h), cases 1-3 remained nearly identical to findings from the main text (Table S3; figs. S30–32). Therefore, our findings in the main text are not affected by the considerable weight of Lena and GBJD in our dataset.

River deltas like GBJD can receive sediment from marine sources via tides, which may affect the area-to-length scaling relationship observed here. We then performed a similar sensitivity analysis by examining a subset of data of only river-dominated deltas (479 out of 5892 data points used). Still, we found no deviation from the main finding: the coefficient is 1.39, and the exponent is 0.62 (fig. S33; Table S3). The overall statistic of h shows a minor change in magnitude but maintains a similar trend (fig. S34; Table S3). In summary of all the above sensitivity analyses, our finding in the main text is robust across delta networks of different types. However, we note that the impact of tidal forcing on the delta network is a key area for future work to explain the location and formation mechanisms of the scale breaks.

Shoreline Spacing Metrics

The Euclidean distance is measured between each outlet (L_e) for shoreline spacing. Normalized spacing (L_o) is calculated by dividing the sum of the Euclidean distances by a proxy for shoreline length (inspired by *29*) : $L_o = L_e \Big/ \sum_n L_e$. The delta shoreline length is not a well-defined quantity (*29*), and there is currently no consensus on a standard method; thus, the sum of Euclidean distances is used for simplicity and can also be viewed as a long-wavelength-filtered shoreline length.

Fig. S1.

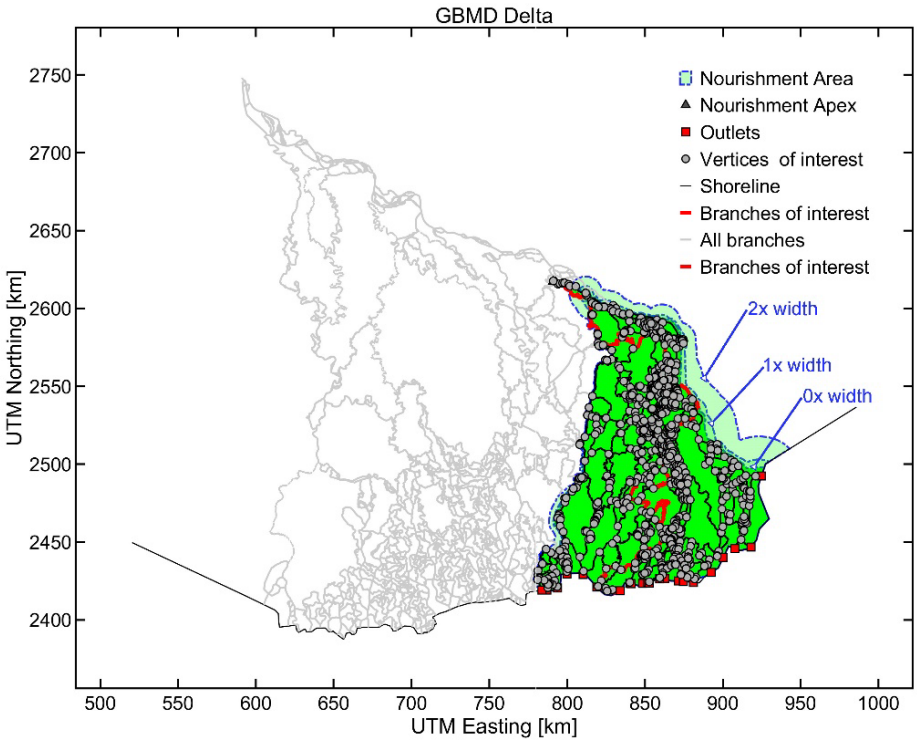

Maps showing the delineation of the nourishment area and the three perimeter buffers, as well as the channel length for the Ganges-Brahmaputra-Jamuna delta (GBJD).

Fig. S2.

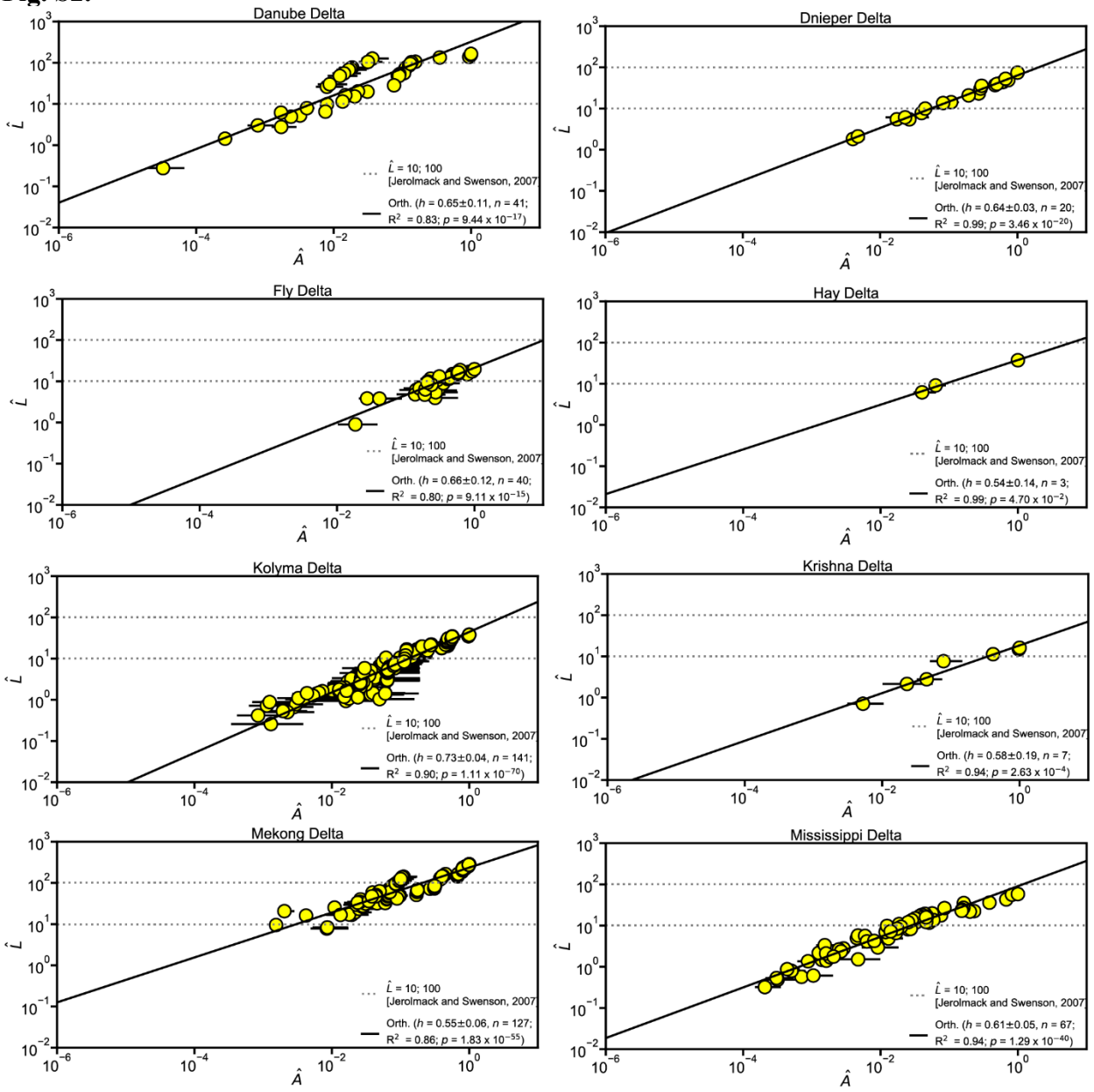

Scaling law of normalized nourishment area ($\widehat{A}$) versus the length of the longest distributary channel ($\widehat{L}$) for each Uniform Delta Network. Herein, the nourishment area is normalized by the delta area, and the channel width of the main branch normalizes the distributary channel length.

Fig. S3.

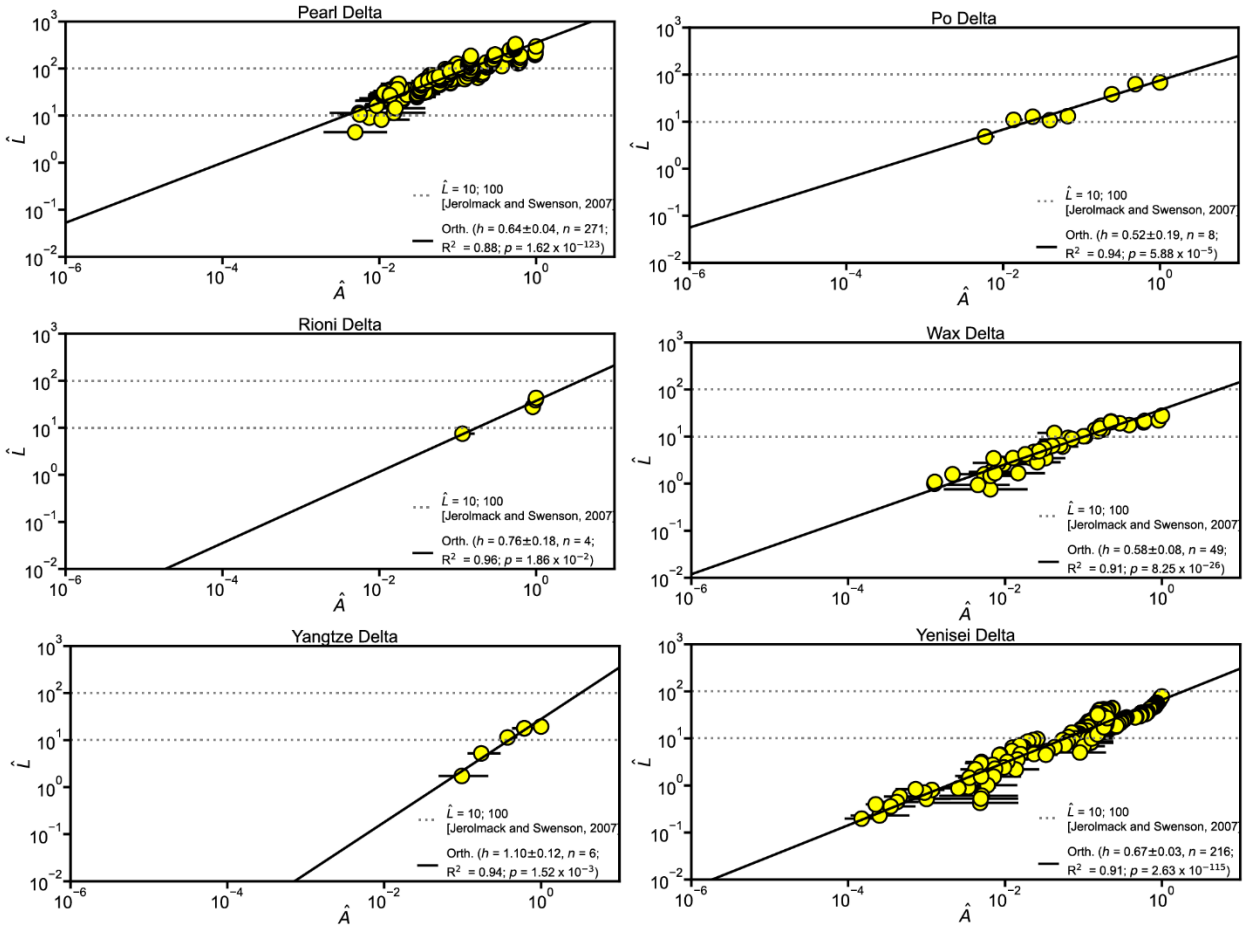

Scaling law of normalized nourishment area ($\widehat{A}$) versus the length of the longest distributary channel ($\widehat{L}$) for each Uniform Delta Network. Herein, the nourishment area is normalized by the delta area, and the channel width of the main branch normalizes the distributary channel length.

Fig. S4.

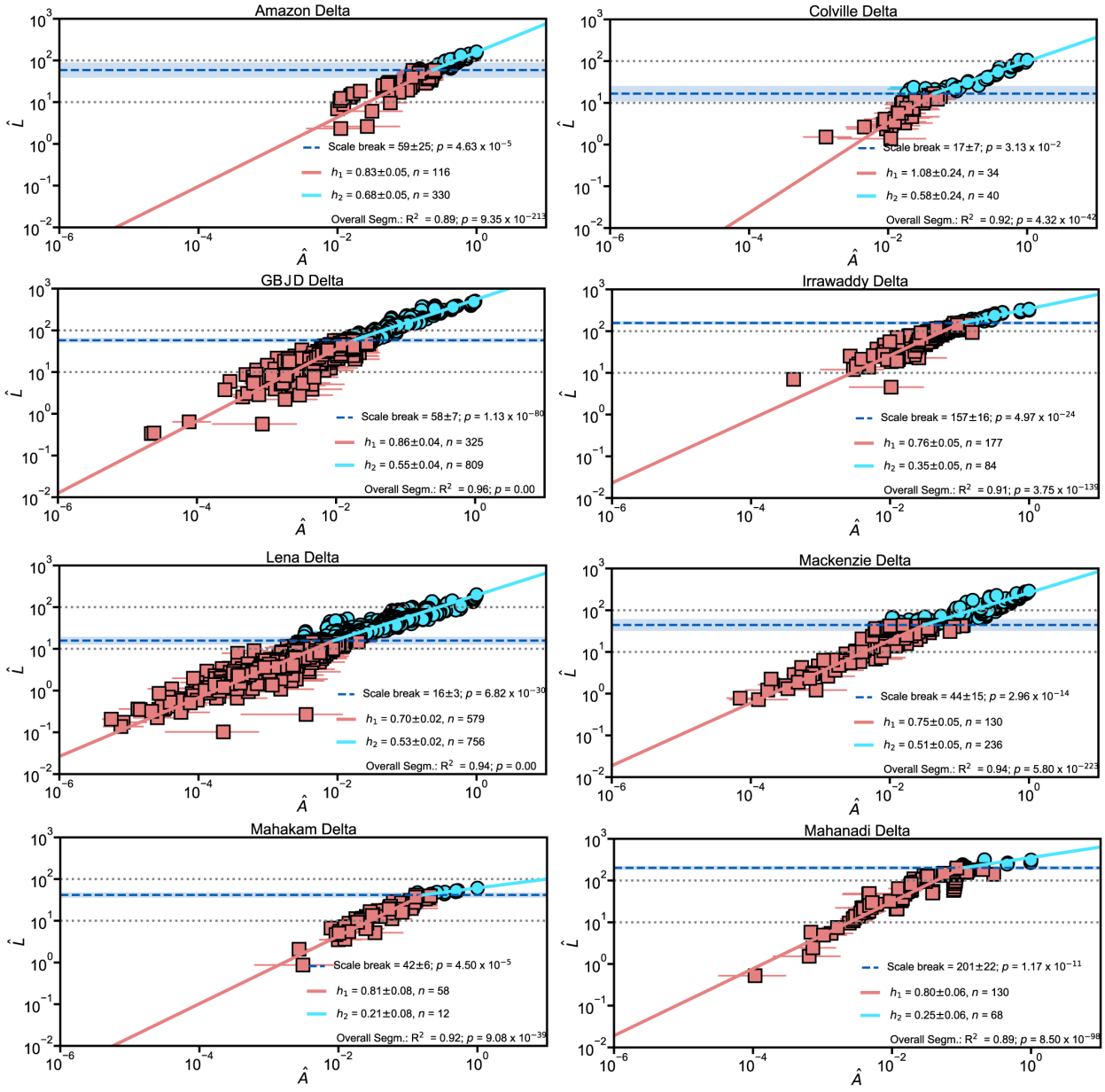

Scaling law of normalized nourishment area ($\widehat{A}$) versus the length of the longest distributary channel ($\widehat{L}$) for each Composite Delta Network. Herein, the nourishment area is normalized by the delta area, and the channel width of the main branch normalizes the distributary channel length.

Fig. S5.

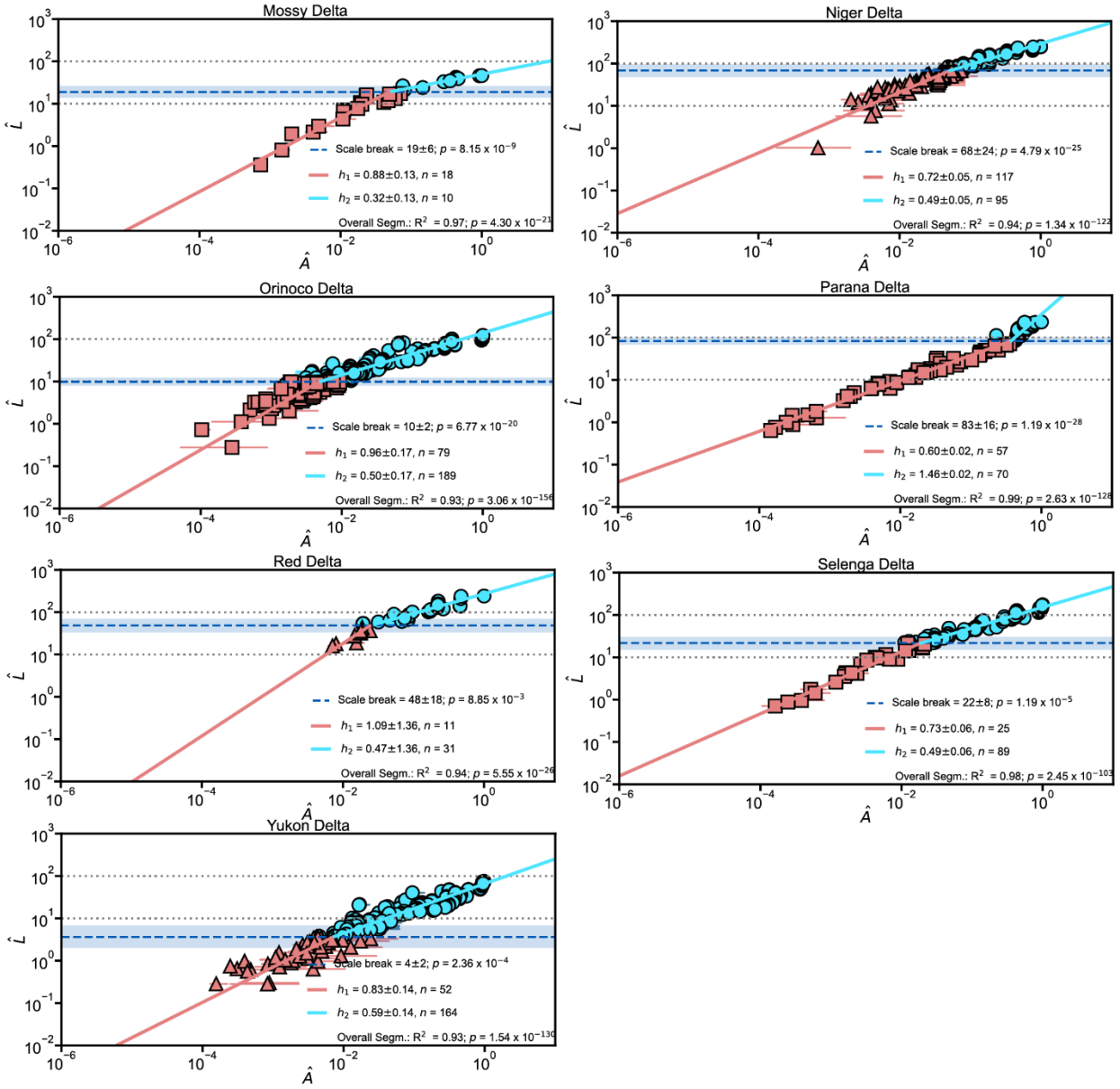

Scaling law of normalized nourishment area ($\widehat{A}$) versus the length of the longest distributary channel ($\widehat{L}$) for each Composite Delta Network. Herein, the nourishment area is normalized by the delta area, and the channel width of the main branch normalizes the distributary channel length.

Fig. S6.

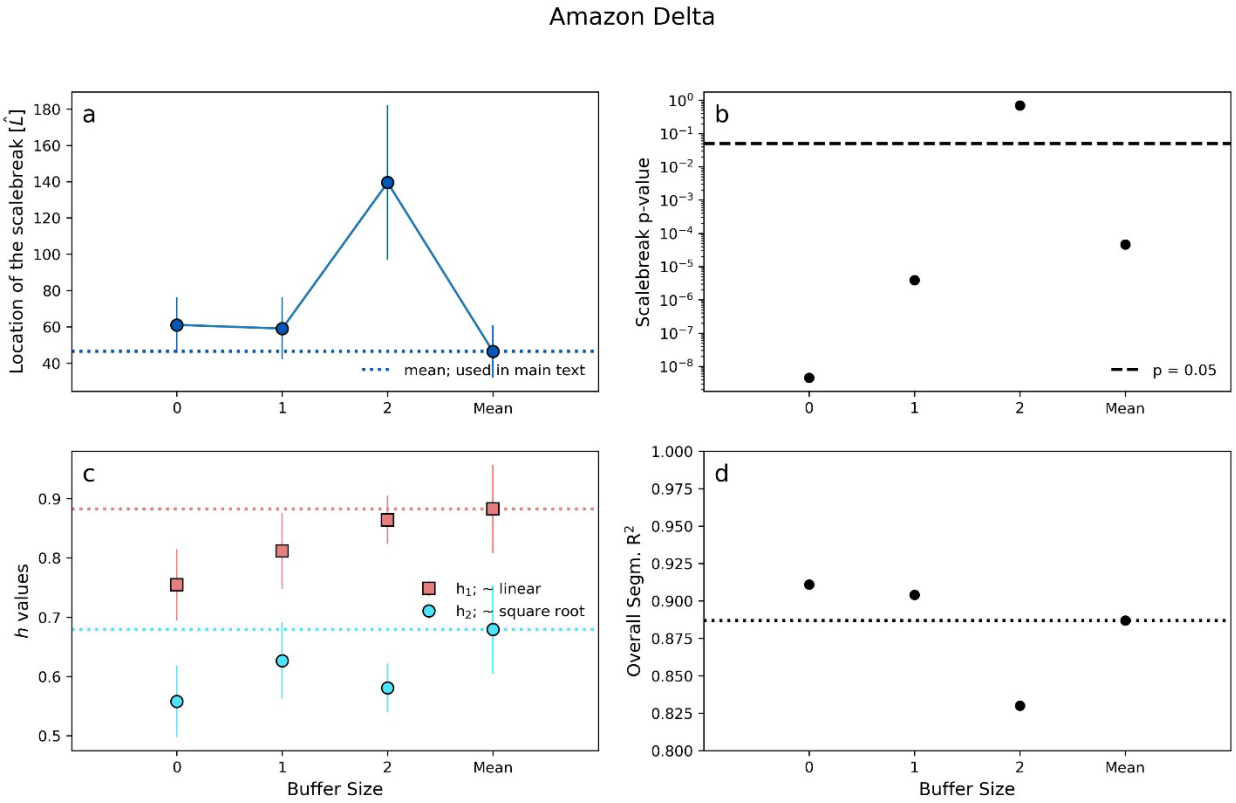

Sensitivity analysis of the scale break for Amazon Delta. The plot panels show a) the location and b) the statistical significance (p-value) of the scale break, c) the exponents (*h* values), and d) the coefficient of determination (R^2) from the power-law relationship between the longest distributary channel length and nourishment area, with different buffer sizes. Here, the buffers are 0x, 1x, and 2x the local channel width to account for uncertainty in overbank transport of bed material sand. Means are the values used in the main text. Additionally, a randomly distributed error ranging from 1% to 5% was added to the channel length to account for measurement uncertainty. Horizontal dashed lines in panels c and d are mean values from the main text.

Fig. S7.

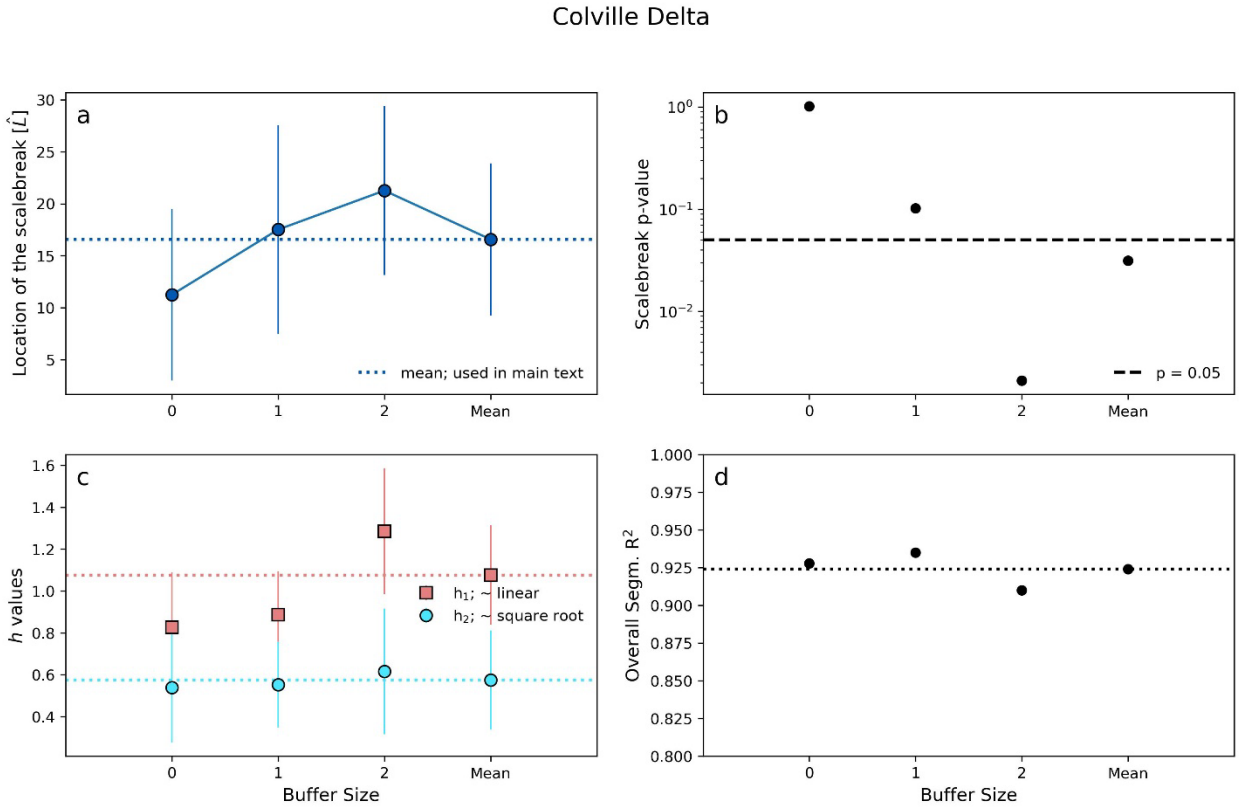

Sensitivity analysis of the scale break for Colville Delta. The plot panels show a) the location and b) the statistical significance (p-value) of the scale break, c) the exponents (*h* values), and d) the coefficient of determination (R^2) from the power-law relationship between the longest distributary channel length and nourishment area, with different buffer sizes. Here, the buffers are 0x, 1x, and 2x the local channel width to account for uncertainty in overbank transport of bed material sand. Means are the values used in the main text. Additionally, a randomly distributed error ranging from 1% to 5% was added to the channel length to account for measurement uncertainty. Horizontal dashed lines in panels c and d are mean values from the main text.

Fig. S8.

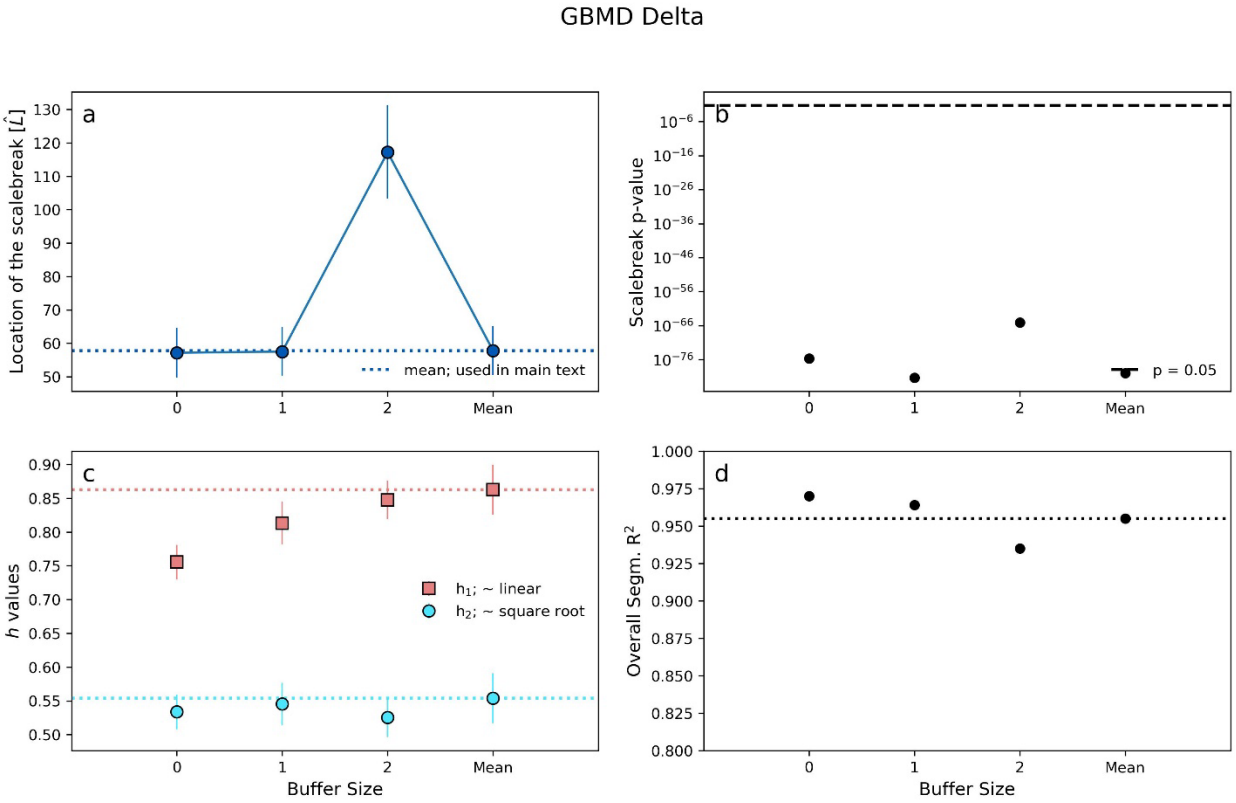

Sensitivity analysis of the scale break for the Ganges-Brahmaputra-Jamuna delta (GBJD). The plot panels show a) the location and b) the statistical significance (p-value) of the scale break, c) the exponents (*h* values), and d) the coefficient of determination (R^2) from the power-law relationship between the longest distributary channel length and nourishment area, with different buffer sizes. Here, the buffers are 0x, 1x, and 2x the local channel width to account for uncertainty in overbank transport of bed material sand. Means are the values used in the main text. Additionally, a randomly distributed error ranging from 1% to 5% was added to the channel length to account for

measurement uncertainty. Horizontal dashed lines in panels c and d are mean values from the main text.

Fig. S9.

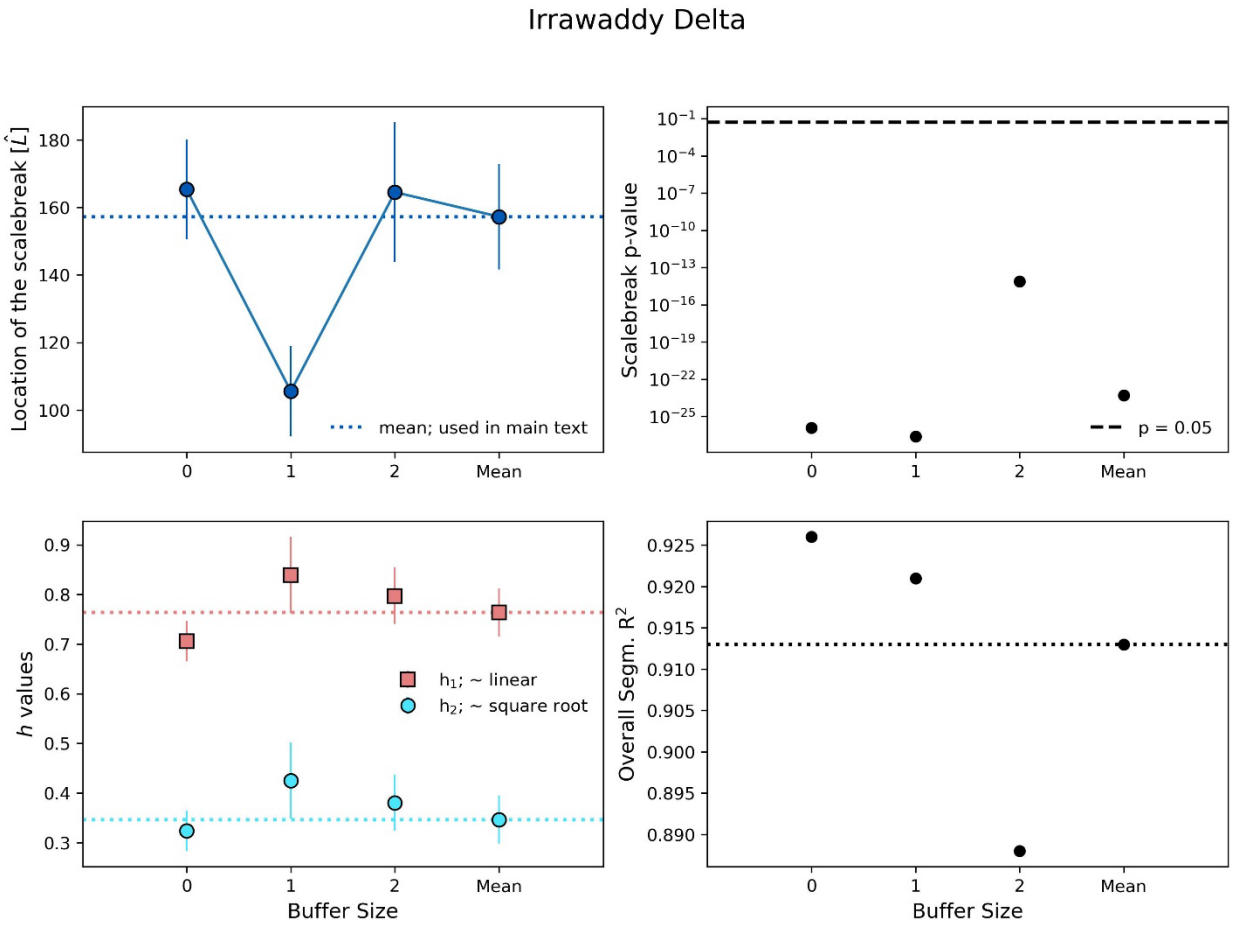

Sensitivity analysis of the scale break for the Irrawaddy Delta. The plot panels show a) the location and b) the statistical significance (p-value) of the scale break, c) the exponents (*h* values), and d) the coefficient of determination (R^2) from the power-law relationship between the longest distributary channel length and nourishment area, with different buffer sizes. Here, the buffers are 0x, 1x, and 2x the local channel width to account for uncertainty in overbank transport of bed material sand. Means are the values used in the main text. Additionally, a randomly distributed error ranging from 1% to 5% was added to the channel length to account for measurement uncertainty. Horizontal dashed lines in panels c and d are mean values from the main text.

Fig. S11.

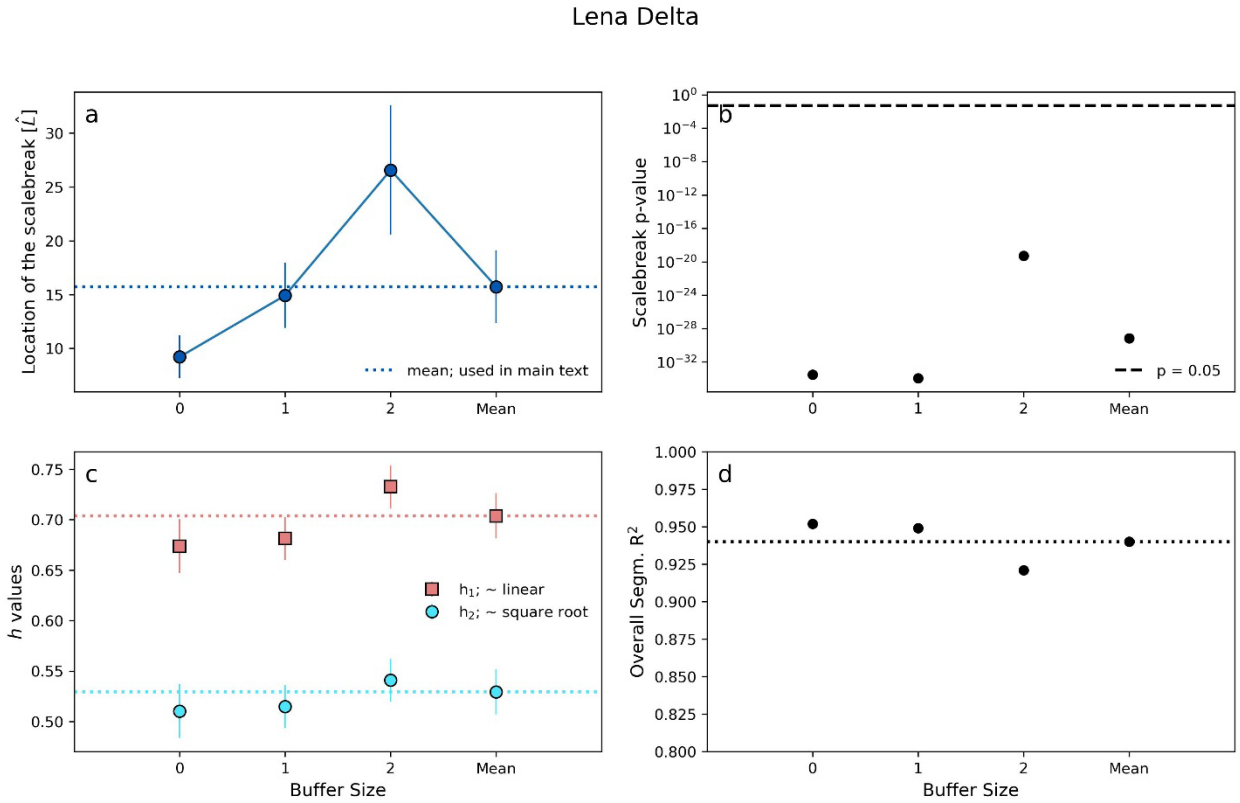

Sensitivity analysis of the scale break for the Lena Delta. The plot panels show a) the location and b) the statistical significance (p-value) of the scale break, c) the exponents (*h* values), and d) the coefficient of determination (R^2) from the power-law relationship between the longest distributary channel length and nourishment area, with different buffer sizes. Here, the buffers are 0x, 1x, and 2x the local channel width to account for uncertainty in overbank transport of bed material sand. Means are the values used in the main text. Additionally, a randomly distributed error ranging from 1% to 5% was added to the channel length to account for measurement uncertainty. Horizontal dashed lines in panels c and d are mean values from the main text.

Fig. S12.

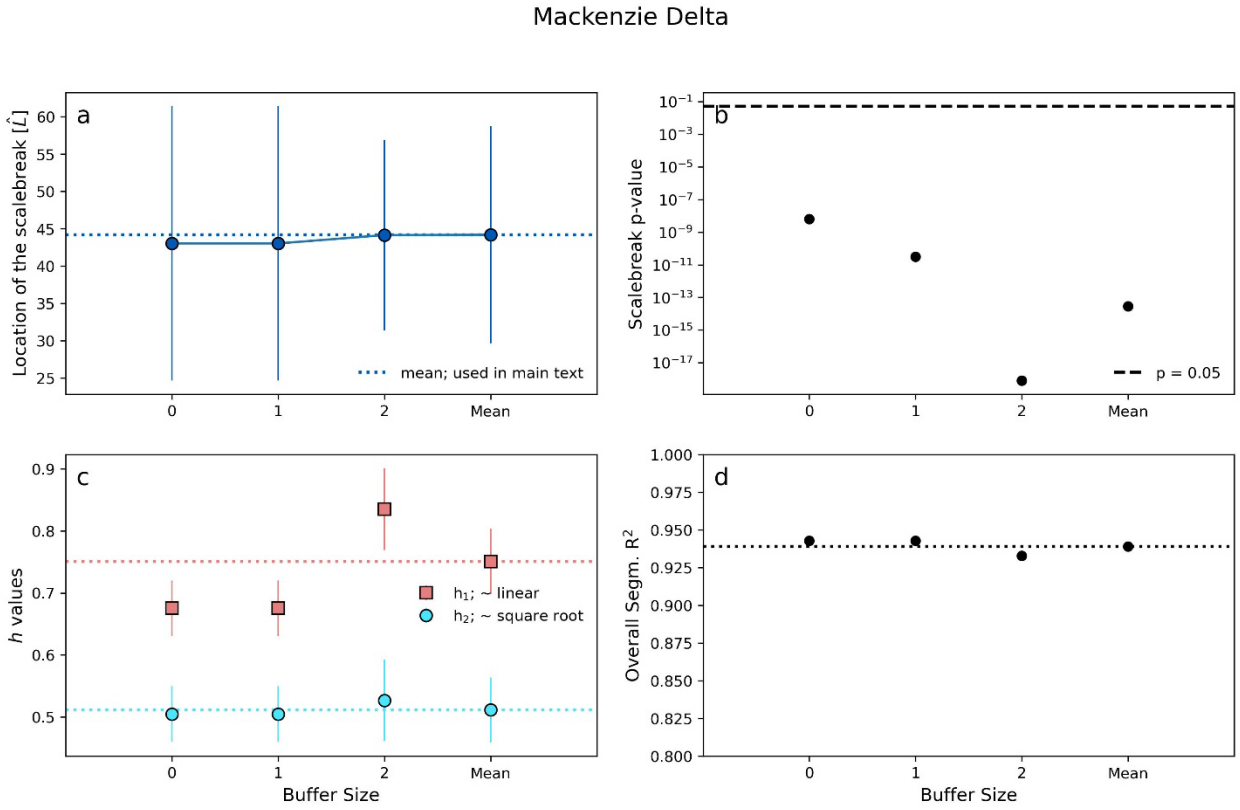

Sensitivity analysis of the scale break for the Mackenzie Delta. The plot panels show a) the location and b) the statistical significance (p-value) of the scale break, c) the exponents (*h* values), and d) the coefficient of determination (R^2) from the power-law relationship between the longest distributary channel length and nourishment area, with different buffer sizes. Here, the buffers are 0x, 1x, and 2x the local channel width to account for uncertainty in overbank transport of bed material sand. Means are the values used in the main text. Additionally, a randomly distributed error ranging from 1% to 5% was added to the channel length to account for measurement uncertainty. Horizontal dashed lines in panels c and d are mean values from the main text.

Fig. S13.

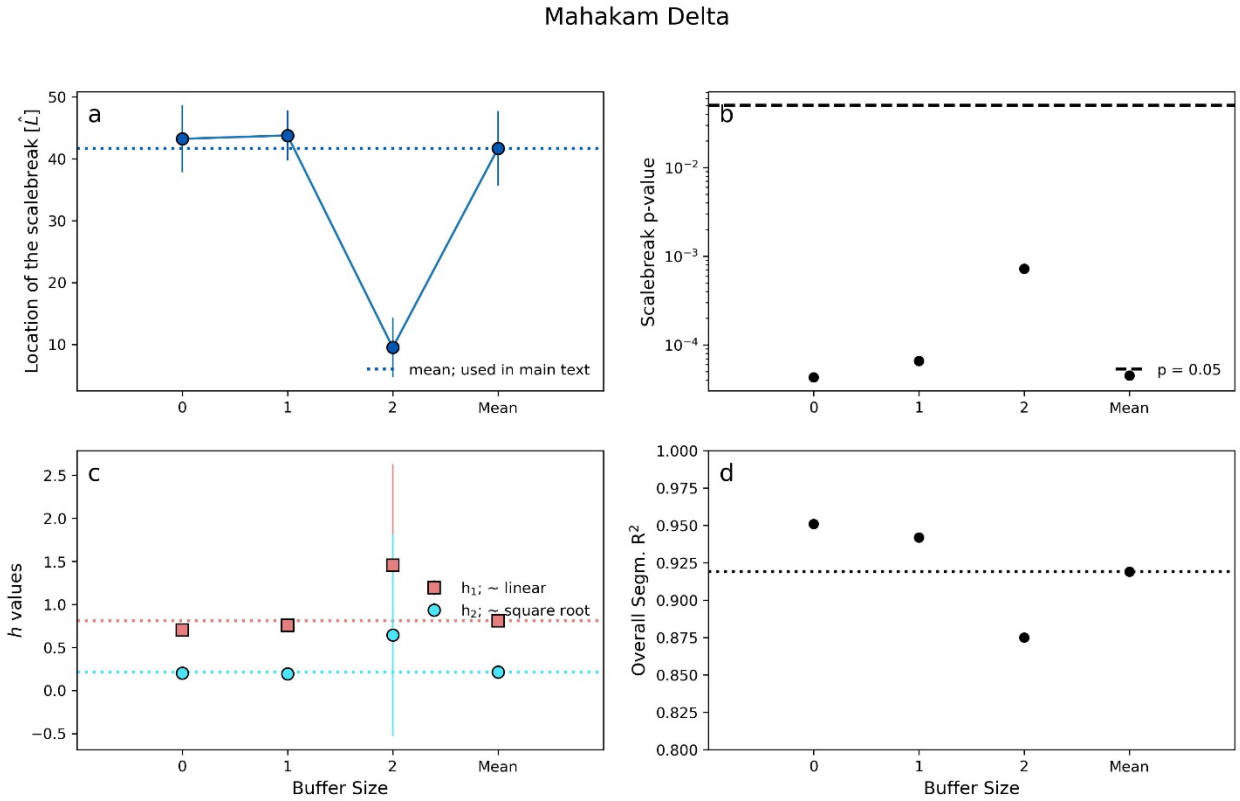

Sensitivity analysis of the scale break for the Mahakam Delta. The plot panels show a) the location and b) the statistical significance (p-value) of the scale break, c) the exponents (*h* values), and d) the coefficient of determination (R^2) from the power-law relationship between the longest distributary channel length and nourishment area, with different buffer sizes. Here, the buffers are 0x, 1x, and 2x the local channel width to account for uncertainty in overbank transport of bed material sand. Means are the values used in the main text. Additionally, a randomly distributed error ranging from 1% to 5% was added to the channel length to account for measurement uncertainty. Horizontal dashed lines in panels c and d are mean values from the main text.

Fig. S14.

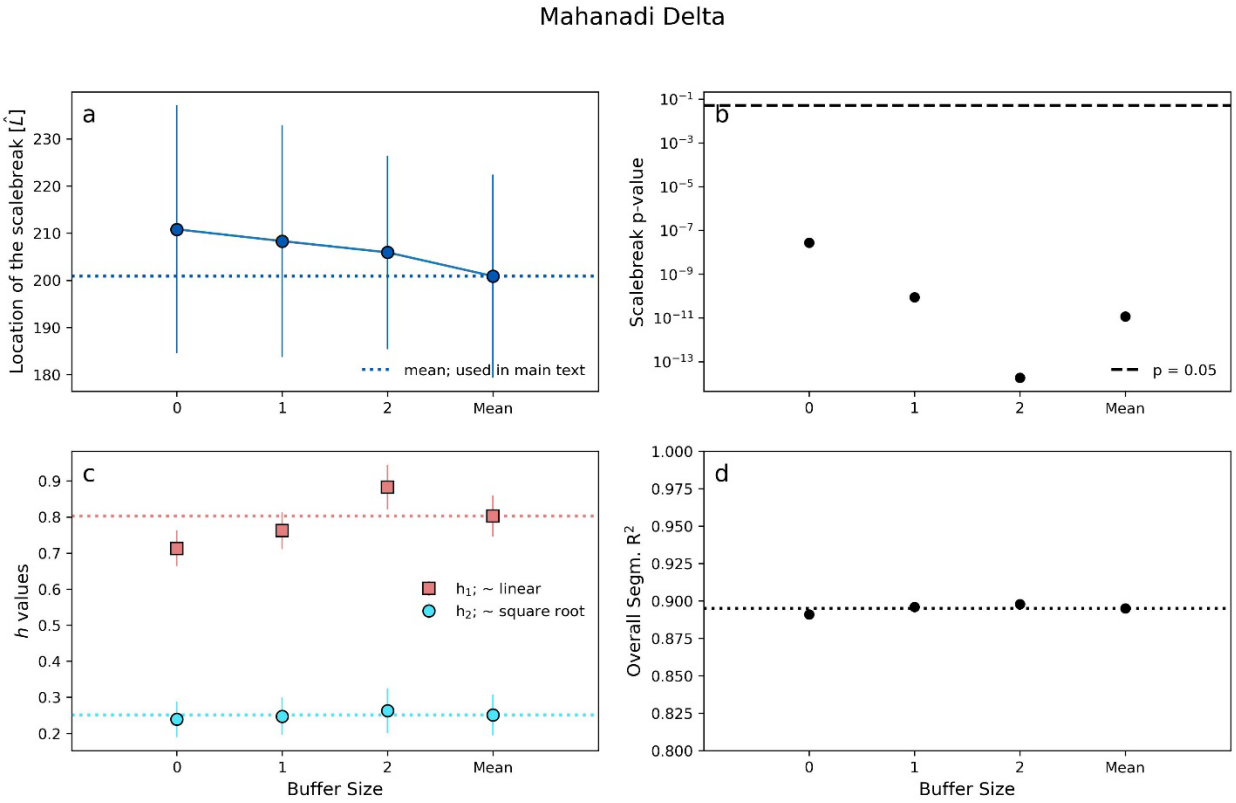

Sensitivity analysis of the scale break for the Mahanadi Delta. The plot panels show a) the location and b) the statistical significance (p-value) of the scale break, c) the exponents (*h* values), and d) the coefficient of determination (R^2) from the power-law relationship between the longest distributary channel length and nourishment area, with different buffer sizes. Here, the buffers are 0x, 1x, and 2x the local channel width to account for uncertainty in overbank transport of bed material sand. Means are the values used in the main text. Additionally, a randomly distributed error ranging from 1% to 5% was added to the channel length to account for measurement uncertainty. Horizontal dashed lines in panels c and d are mean values from the main text.

Fig. S15.

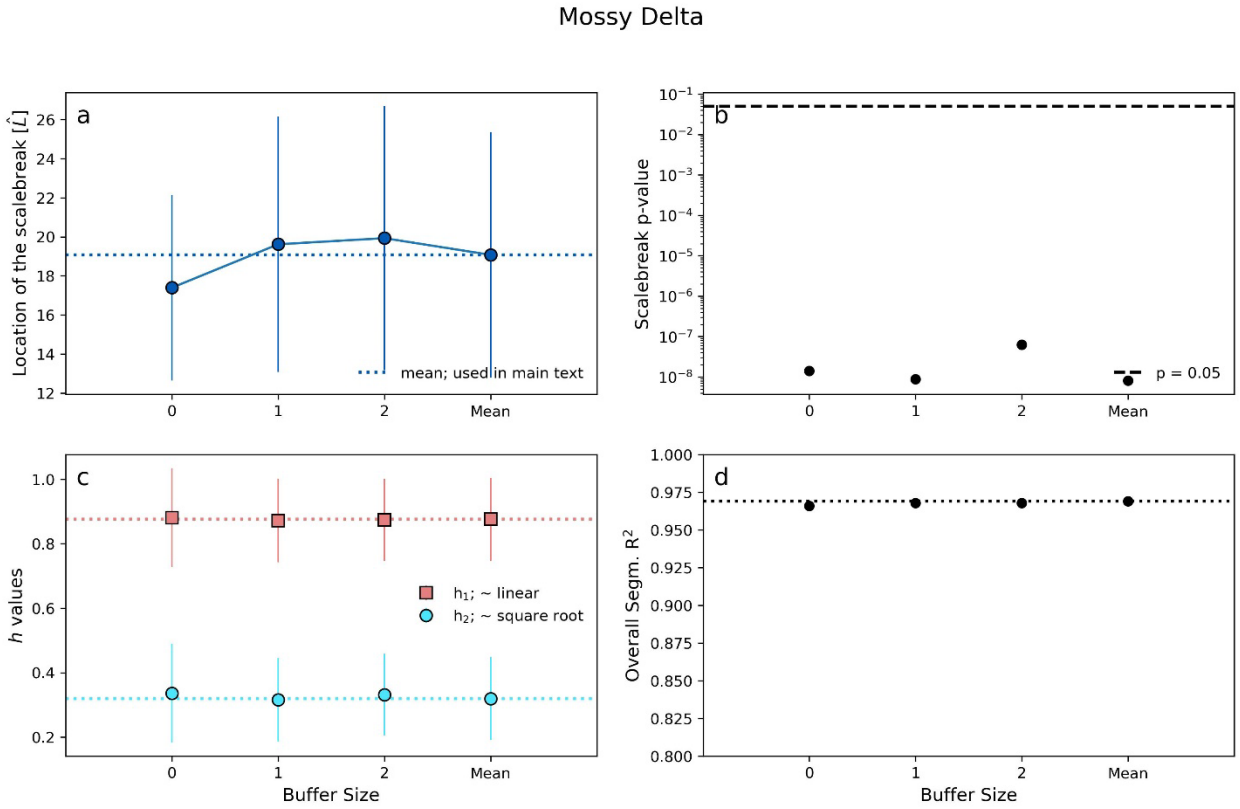

Sensitivity analysis of the scale break for the Mossy Delta. The plot panels show a) the location and b) the statistical significance (p-value) of the scale break, c) the exponents (*h* values), and d) the coefficient of determination (R^2) from the power-law relationship between the longest distributary channel length and nourishment area, with different buffer sizes. Here, the buffers are 0x, 1x, and 2x the local channel width to account for uncertainty in overbank transport of bed material sand. Means are the values used in the main text. Additionally, a randomly distributed error ranging from 1% to 5% was added to the channel length to account for measurement uncertainty. Horizontal dashed lines in panels c and d are mean values from the main text.

Fig. S16.

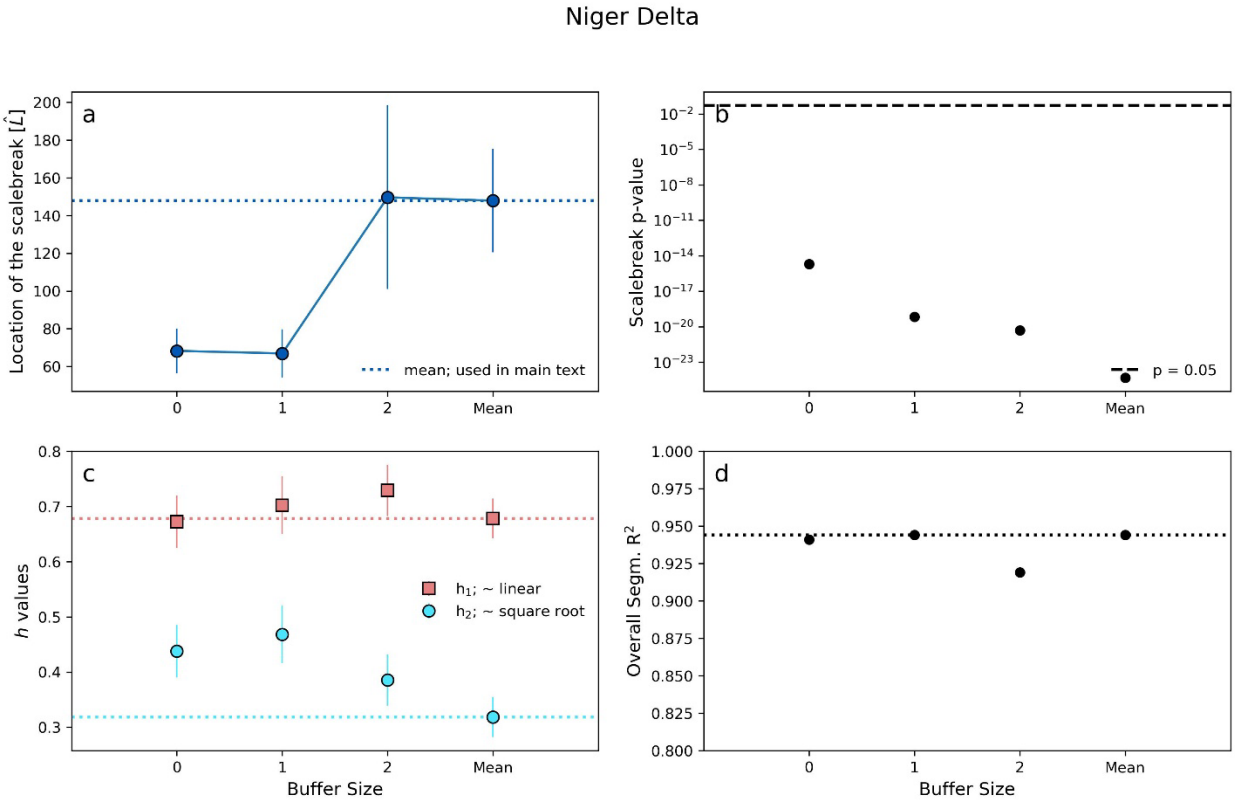

Sensitivity analysis of the scale break for the Niger Delta. The plot panels show a) the location and b) the statistical significance (p-value) of the scale break, c) the exponents (*h* values), and d) the coefficient of determination (R^2) from the power-law relationship between the longest distributary channel length and nourishment area, with different buffer sizes. Here, the buffers are 0x, 1x, and 2x the local channel width to account for uncertainty in overbank transport of bed material sand. Means are the values used in the main text. Additionally, a randomly distributed error ranging from 1% to 5% was added to the channel length to account for measurement uncertainty. Horizontal dashed lines in panels c and d are mean values from the main text.

Fig. S17.

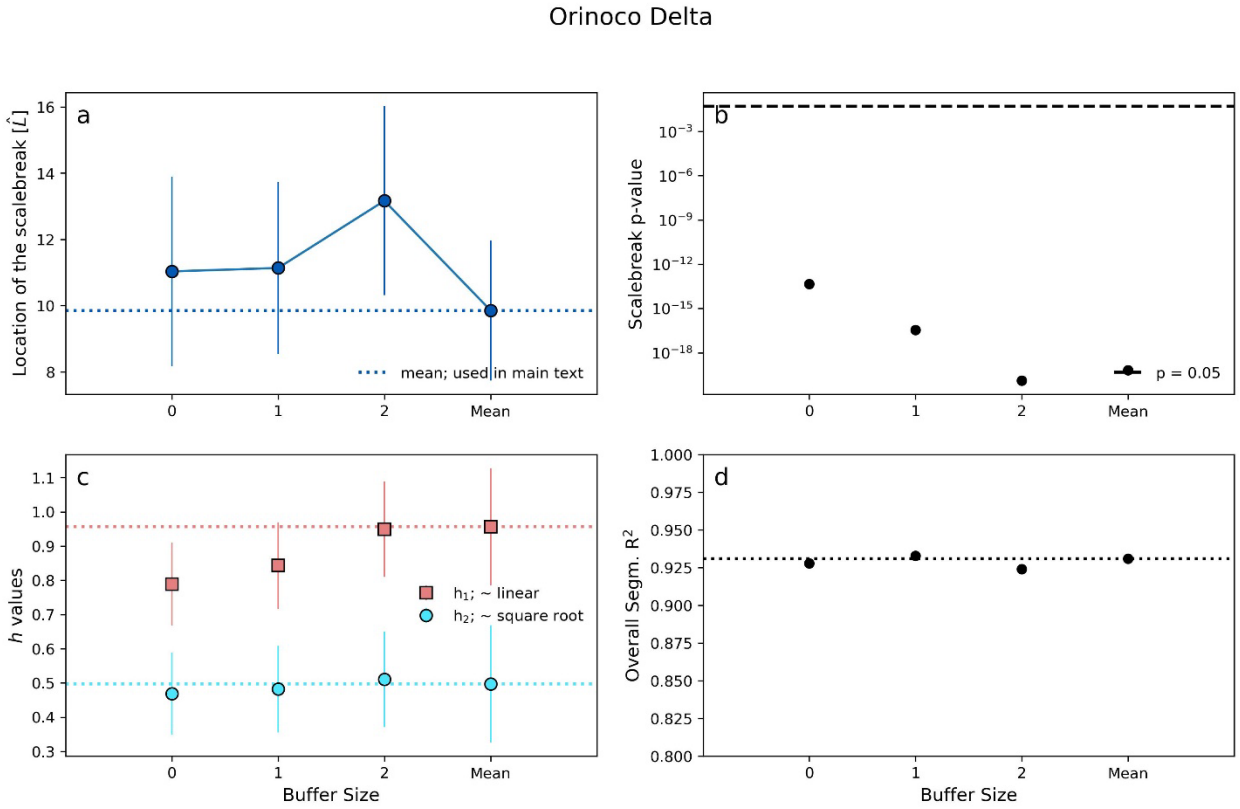

Sensitivity analysis of the scale break for the Orinoco Delta. The plot panels show a) the location and b) the statistical significance (p-value) of the scale break, c) the exponents (*h* values), and d) the coefficient of determination (R^2) from the power-law relationship between the longest distributary channel length and nourishment area, with different buffer sizes. Here, the buffers are 0x, 1x, and 2x the local channel width to account for uncertainty in overbank transport of bed material sand. Means are the values used in the main text. Additionally, a randomly distributed error ranging from 1% to 5% was added to the channel length to account for measurement uncertainty. Horizontal dashed lines in panels c and d are mean values from the main text.

Fig. S18.

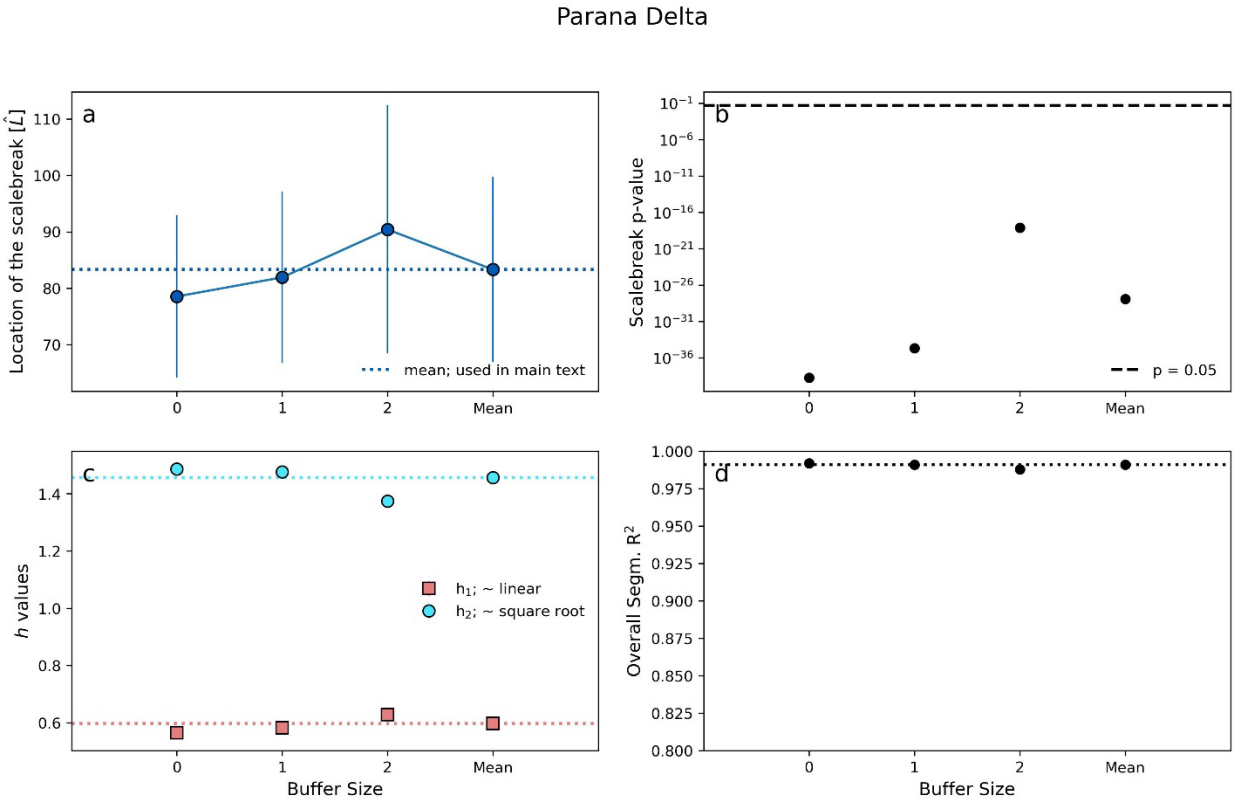

Sensitivity analysis of the scale break for the Parana Delta. The plot panels show a) the location and b) the statistical significance (p-value) of the scale break, c) the exponents (*h* values), and d) the coefficient of determination (R^2) from the power-law relationship between the longest distributary channel length and nourishment area, with different buffer sizes. Here, the buffers are 0x, 1x, and 2x the local channel width to account for uncertainty in overbank transport of bed material sand. Means are the values used in the main text. Additionally, a randomly distributed error ranging from 1% to 5% was added to the channel length to account for measurement uncertainty. Horizontal dashed lines in panels c and d are mean values from the main text.

Fig. S19.

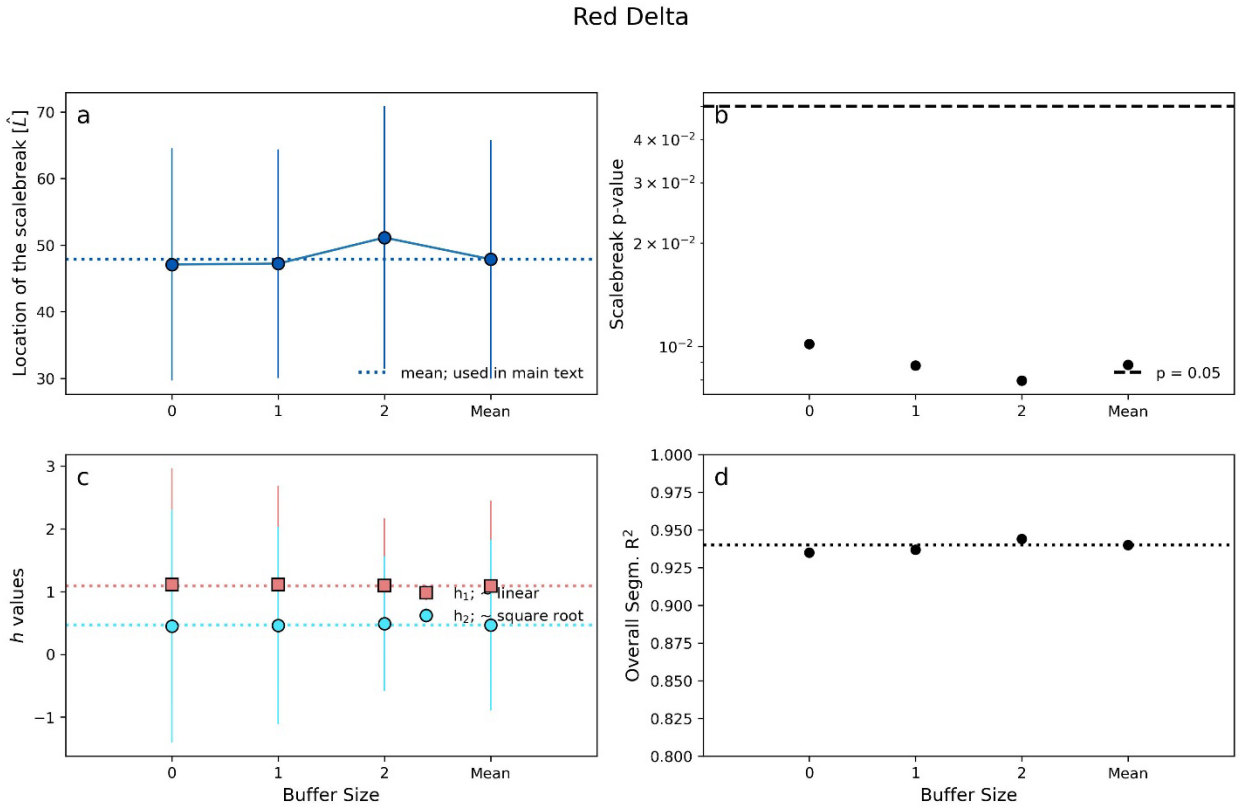

Sensitivity analysis of the scale break for the Red Delta. The plot panels show a) the location and b) the statistical significance (p-value) of the scale break, c) the exponents (*h* values), and d) the coefficient of determination (R^2) from the power-law relationship between the longest distributary channel length and nourishment area, with different buffer sizes. Here, the buffers are 0x, 1x, and 2x the local channel width to account for uncertainty in overbank transport of bed material sand. Means are the values used in the main text. Additionally, a randomly distributed error ranging from 1% to 5% was added to the channel length to account for measurement uncertainty. Horizontal dashed lines in panels c and d are mean values from the main text.

Fig. S20.

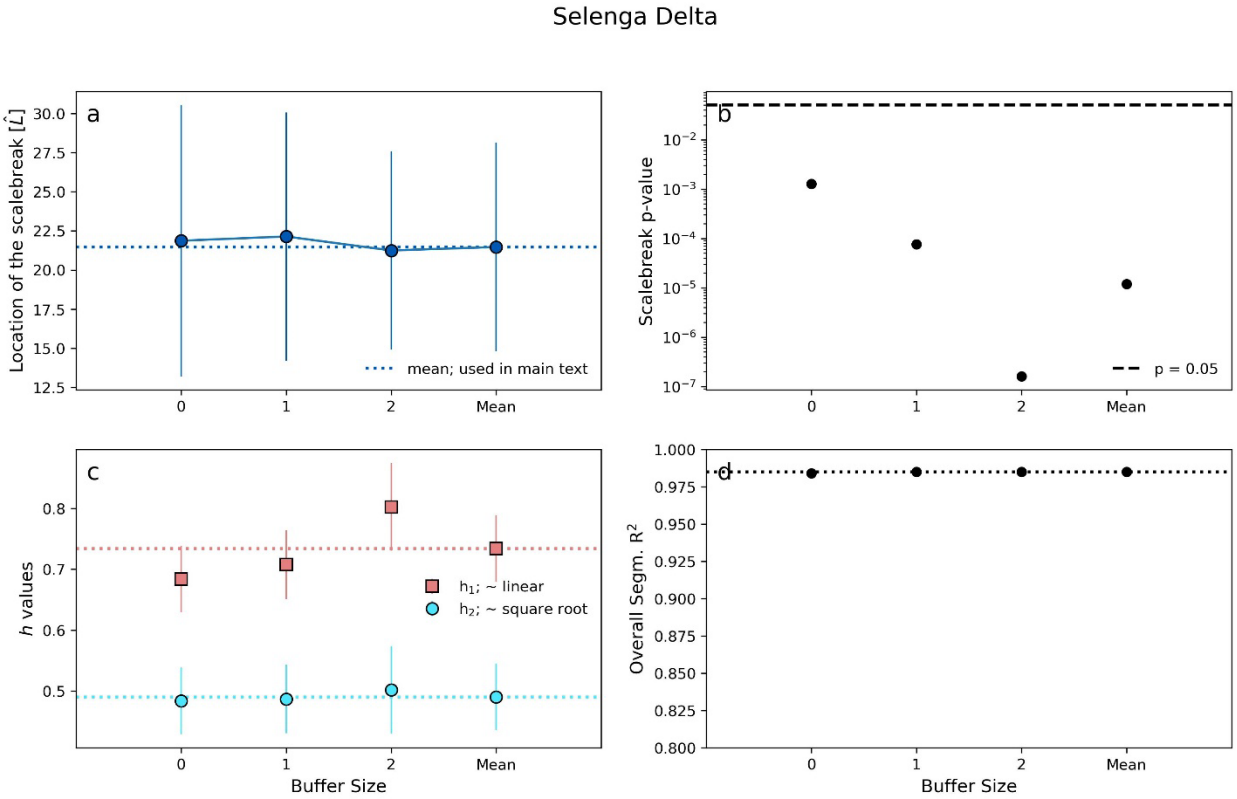

Sensitivity analysis of the scale break for the Selenga Delta. The plot panels show a) the location and b) the statistical significance (p-value) of the scale break, c) the exponents (*h* values), and d) the coefficient of determination (R^2) from the power-law relationship between the longest distributary channel length and nourishment area, with different buffer sizes. Here, the buffers are 0x, 1x, and 2x the local channel width to account for uncertainty in overbank transport of bed material sand. Means are the values used in the main text. Additionally, a randomly distributed error ranging from 1% to 5% was added to the channel length to account for measurement uncertainty. Horizontal dashed lines in panels c and d are mean values from the main text.

Fig. S21.

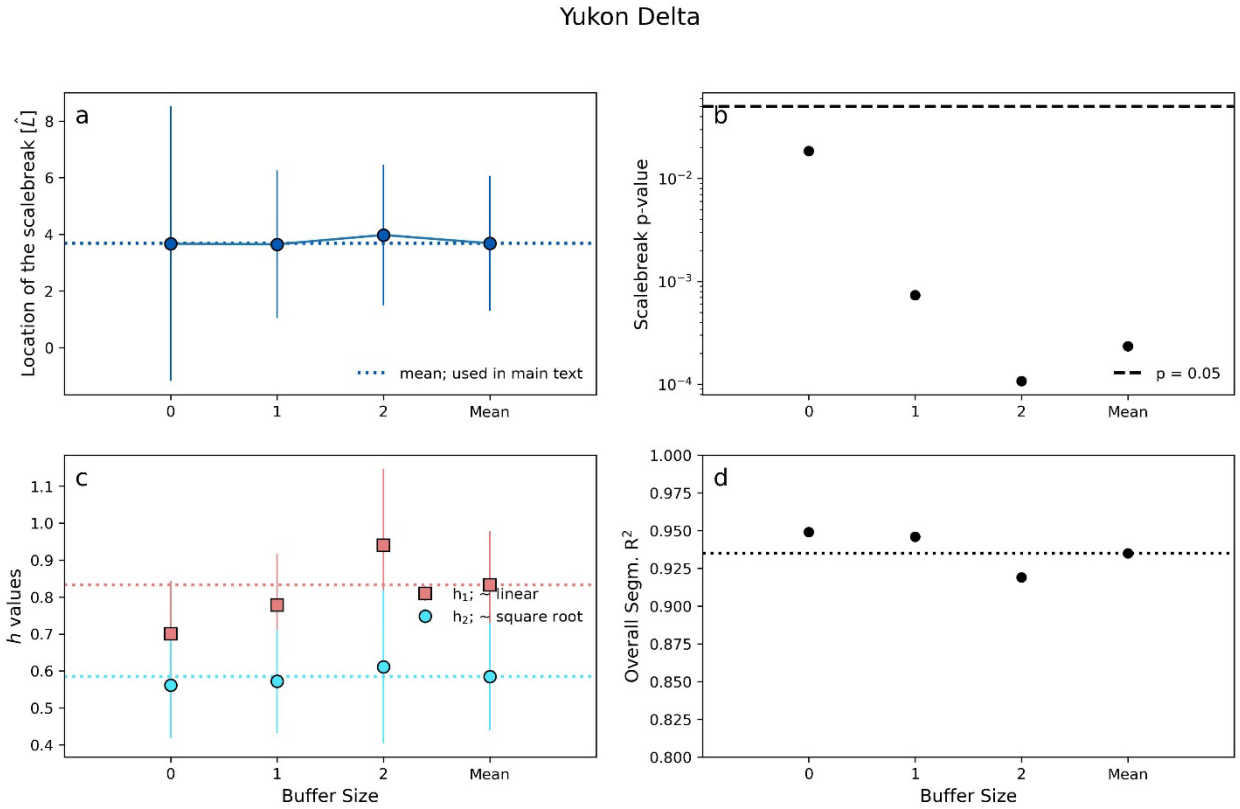

Sensitivity analysis of the scale break for the Yukon Delta. The plot panels show a) the location and b) the statistical significance (p-value) of the scale break, c) the exponents (*h* values), and d) the coefficient of determination (R^2) from the power-law relationship between the longest distributary channel length and nourishment area, with different buffer sizes. Here, the buffers are 0x, 1x, and 2x the local channel width to account for uncertainty in overbank transport of bed material sand. Means are the values used in the main text. Additionally, a randomly distributed error ranging from 1% to 5% was added to the channel length to account for measurement uncertainty. Horizontal dashed lines in panels c and d are mean values from the main text.

Fig. S22.

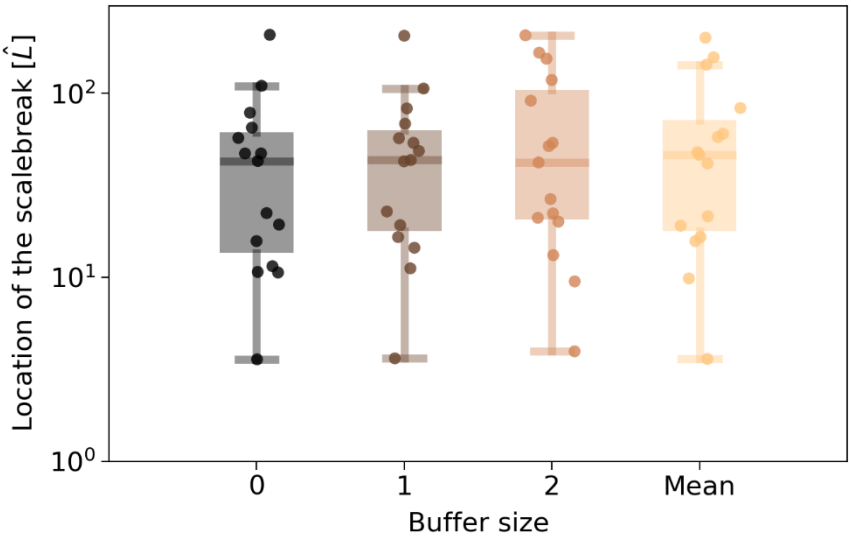

Boxplots showing a summary of the scale break for the different buffer sizes, including 0x, 1x, and 2x the local channel width. Boxes indicate interquartile range (IQR, 75% - 25%), and lines inside the boxes are the medians. Whiskers and caps represent ±1.5× IQR.

Fig. S23.

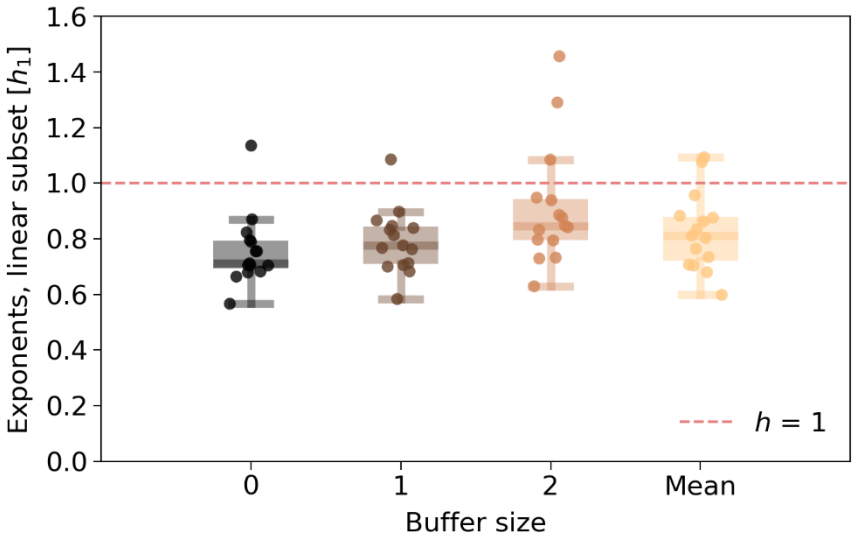

Boxplots showing a summary of the exponents for the quasi-linear subset (h_1) for the different buffer sizes, including 0x, 1x, and 2x the local channel width, and the mean value used in the main text. Boxes indicate interquartile range (IQR, 75% - 25%), and lines inside the boxes are the medians. Whiskers and caps represent ±1.5× IQR.

Fig. S24.

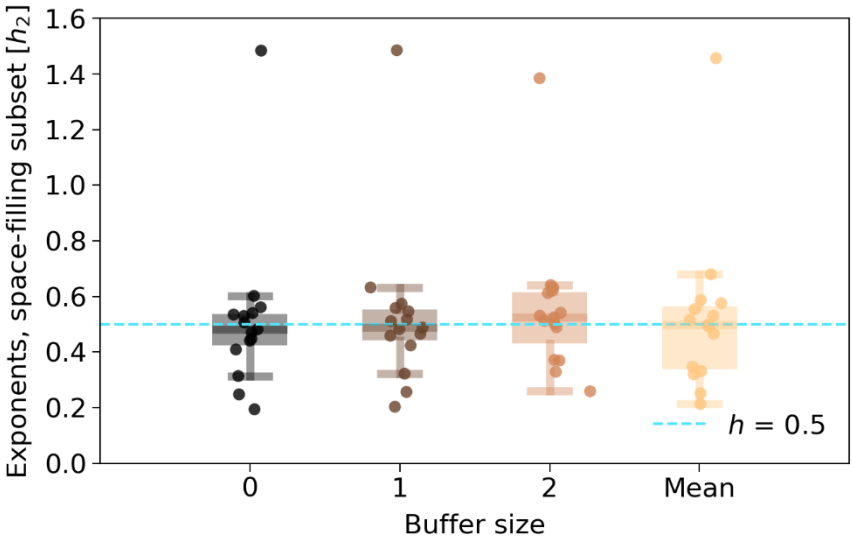

Boxplots showing a summary of the exponents for the space-filling subset (h_2) for the different buffer sizes, including 0x, 1x, and 2x the local channel width, and the mean value used in the main text. Boxes indicate interquartile range (IQR, 75% - 25%), and lines inside the boxes are the medians. Whiskers and caps represent ±1.5× IQR.

Fig. S25.

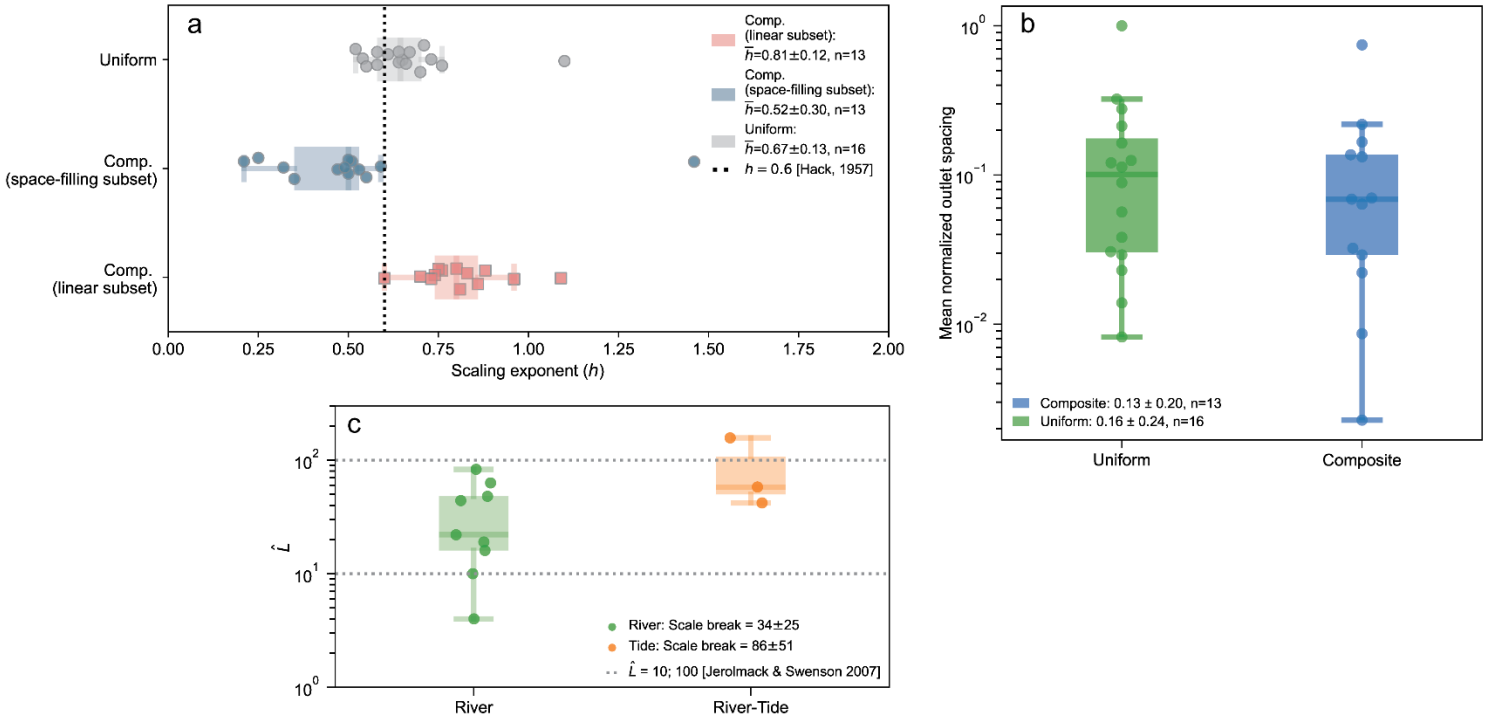

Recalculated plots corresponding to Figure 4A-C in the main text, by removing Amazon and Colville deltas from the Composite Delta Network but keeping them as part of the Uniform Delta Network, are presented here: (a) Scaling exponent *h* for the entire data set across different channel network patterns. *n* represents the amount of data. (b) Mean normalized outlet spacing (L_o) for river deltas with Uniform and Composite Network patterns. (c) locations of the scale break across hydrodynamics as a function of normalized channel length. This test is based on the results of the sensitivity analysis, where some of the p-values of the scale break for these two deltas are greater than 0.05, indicating no statistically significant evidence for the existence of the scale break. Nevertheless, these recalculated values are similar to those presented in the main text and do not impact our conclusions. Boxes in panels B and C indicate interquartile range (IQR, 75% - 25%), and lines inside the boxes are the medians. Whiskers and caps represent ±1.5× IQR**.**

Fig. S26.

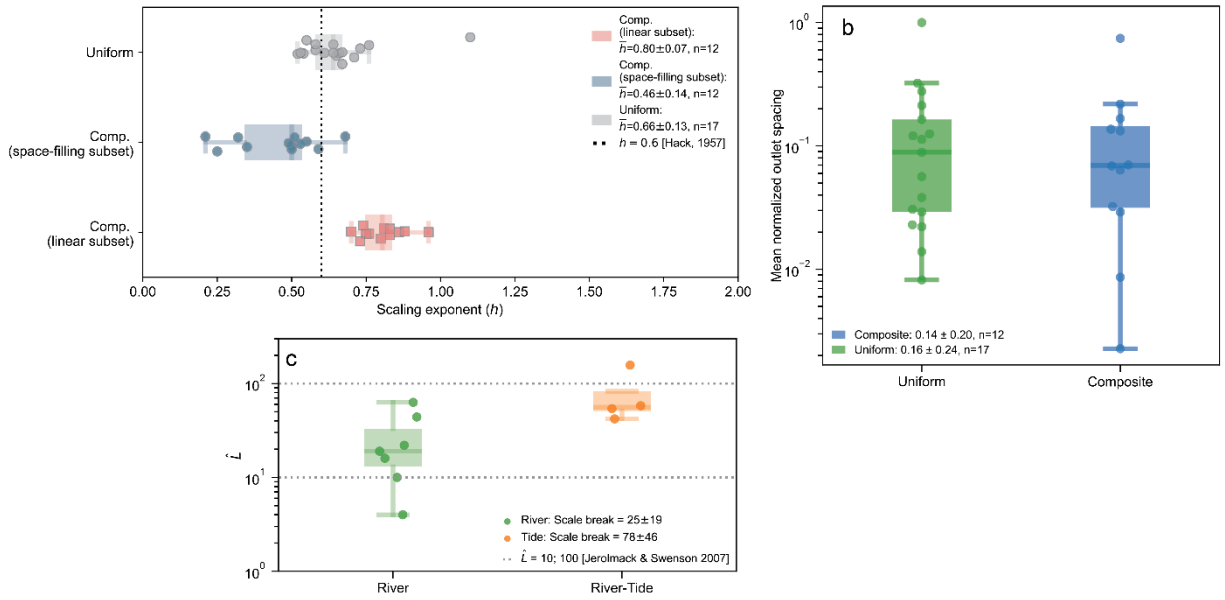

Recalculated plots corresponding to Figure 4A-C in the main text, by removing Colville, Parana, and Red deltas from the Composite Delta Network but keeping them as part of the Uniform Delta Network, are presented here: (a) Scaling exponent *h* for the entire data set across different channel network patterns. *n* represents the amount of data. (b) Mean normalized outlet spacing (L_o) for river deltas with Uniform and Composite Network patterns. (c) locations of the scale break across hydrodynamics as a function of normalized channel length. This test is conducted because these deltas exhibit superlinear scaling relationships, and we want to investigate how they would impact the results. Nevertheless, these recalculated values are similar to those presented in the main text and do not impact our conclusions. Boxes in panels B and C indicate interquartile range (IQR, 75% - 25%), and lines inside the boxes are the medians. Whiskers and caps represent ±1.5× IQR**.**

Fig. S27.

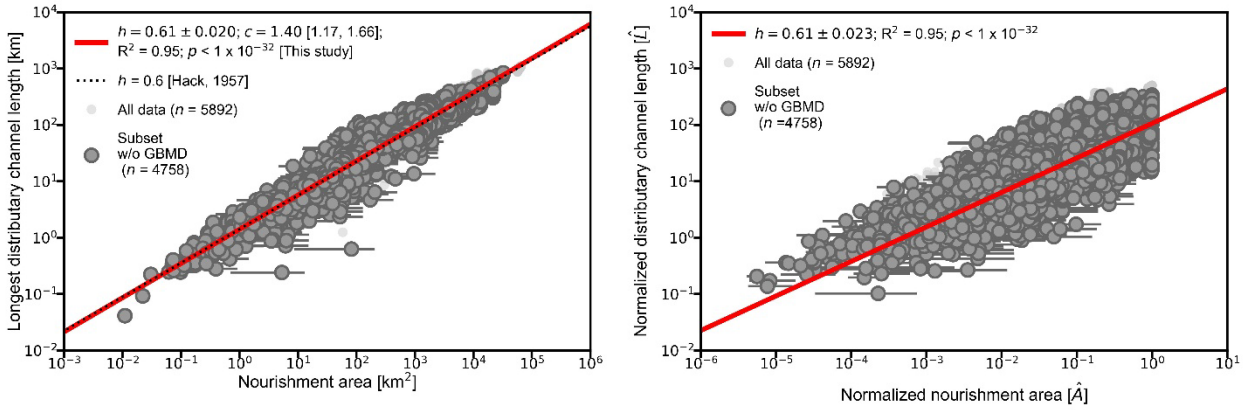

(left) Dimensional and (right) dimensionless scaling law of the distributary channel network of nourishment area (A) and the length (L) of the longest distributary channel in that area, obtained from the dataset without GBJD. R^2 and p-values are reported. Error bars represent the range of A, among 0×, 1×, and 2× local channel width (b), as shown in the buffer area boundary.

Fig. S28.

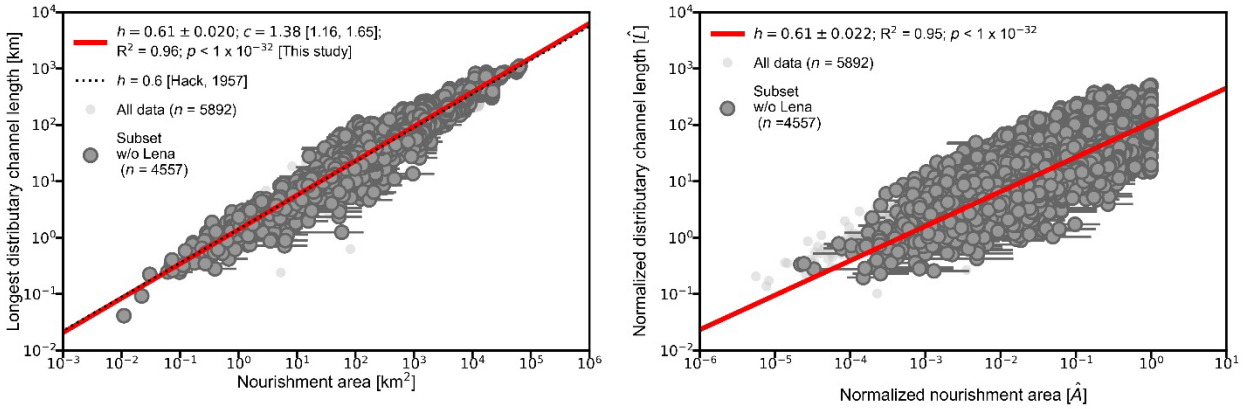

(left) Dimensional and (right) dimensionless scaling law of the distributary channel network of nourishment area (A) and the length (L) of the longest distributary channel in that area, obtained from the dataset without the Lena delta. R^2 and p-values are reported. Error bars represent the range of A, among 0×, 1×, and 2× local channel width (b), as shown in the buffer area boundary.

Fig. S29.

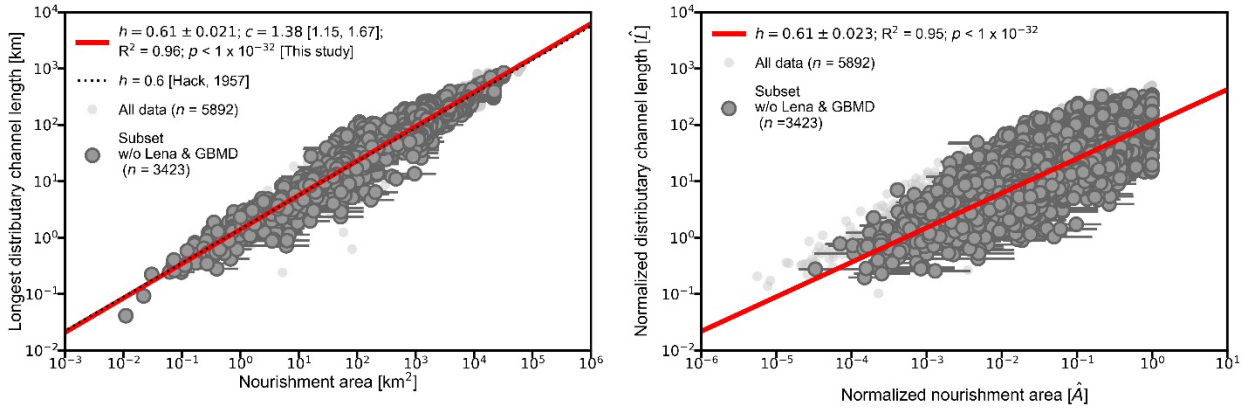

(left) Dimensional and (right) dimensionless scaling law of the distributary channel network of nourishment area (A) and the length (L) of the longest distributary channel in that area, obtained from the dataset without both GBJD and the Lena deltas. R^2 and p-values are reported. Error bars represent the range of A, among 0×, 1×, and 2× local channel width (b), as shown in the buffer area boundary.

Fig. S30.

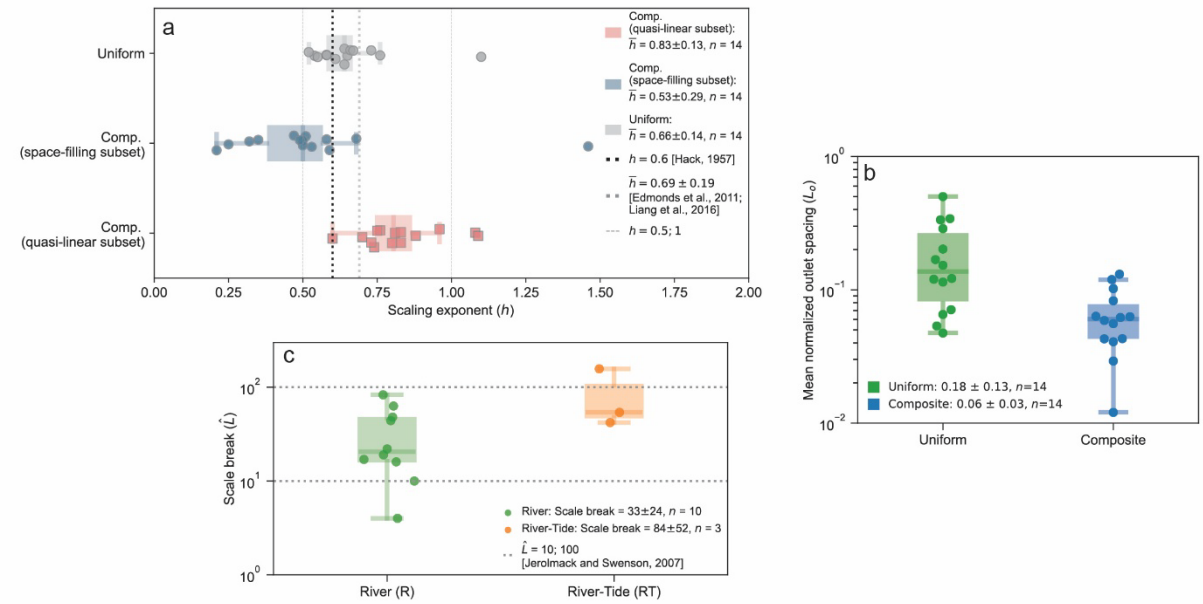

Recalculated plots corresponding to Figure 4A-C in the main text, by removing GBJD from the analysis, are presented here: (a) Scaling exponent *h* for the entire data set across different channel network patterns. *n* represents the amount of data. (b) Mean normalized outlet spacing (L_o) for river deltas with Uniform and Composite Network patterns. (c) locations of the scale break across hydrodynamics as a function of normalized channel length. This test examines the impact of delta size bias. Nevertheless, these recalculated values are similar to those presented in the main text and do not impact our conclusions. Boxes in panels B and C indicate interquartile range (IQR, 75% - 25%), and lines inside the boxes are the medians. Whiskers and caps represent ±1.5× IQR**.**

Fig. S31.

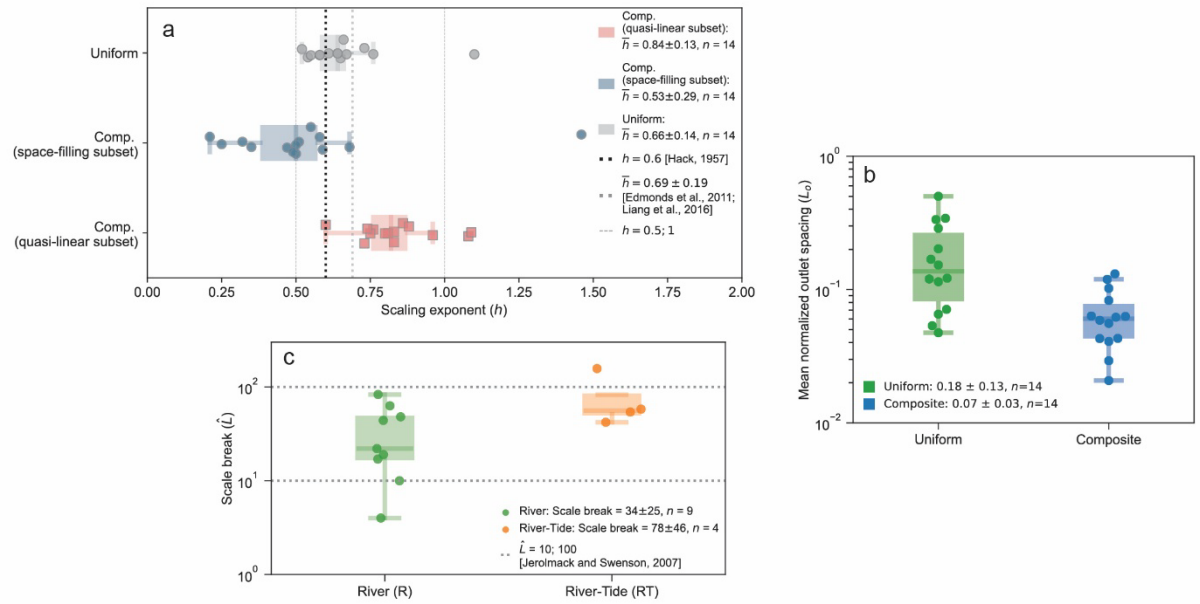

Recalculated plots corresponding to Figure 4A-C in the main text, by removing Lena delta from the analysis, are presented here: (a) Scaling exponent *h* for the entire data set across different channel network patterns. *n* represents the amount of data. (b) Mean normalized outlet spacing (L_o) for river deltas with Uniform and Composite Network patterns. (c) locations of the scale break across hydrodynamics as a function of normalized channel length. This test examines the impact of delta size bias. Nevertheless, these recalculated values are similar to those presented in the main text and do not impact our conclusions. Boxes in panels B and C indicate interquartile range (IQR, 75% - 25%), and lines inside the boxes are the medians. Whiskers and caps represent ±1.5× IQR**.**

Fig. S32.

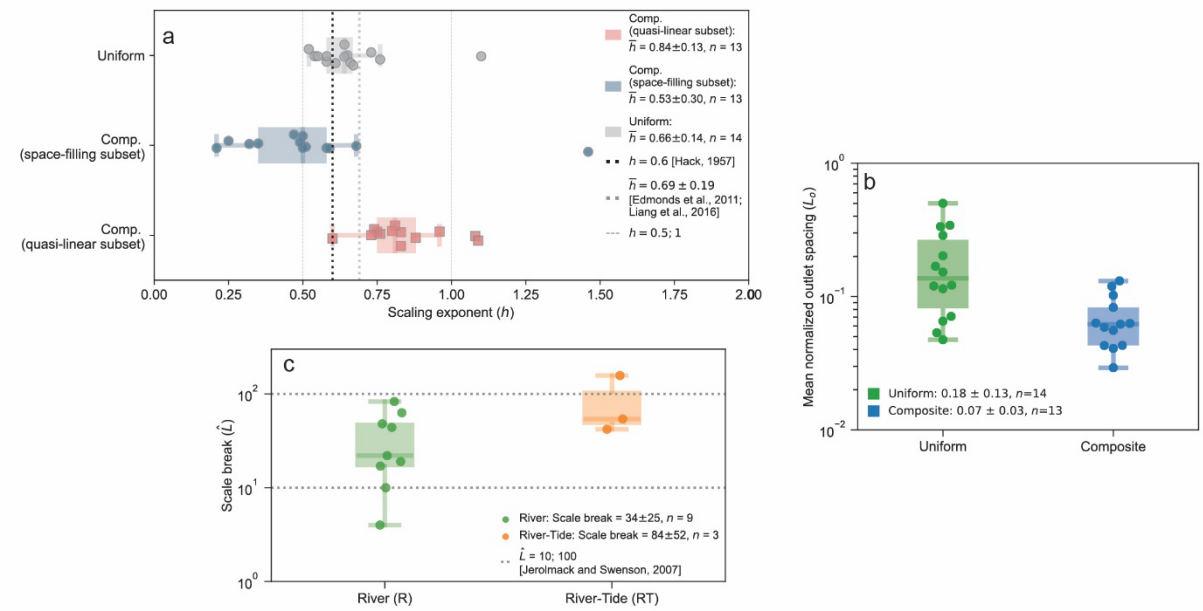

Recalculated plots corresponding to Figure 4A-C in the main text, by removing both the GBJD and Lena deltas from the analysis, are presented here: (a) Scaling exponent *h* for the entire data set across different channel network patterns. *n* represents the amount of data. (b) Mean normalized outlet spacing (L_o) for river deltas with Uniform and Composite Network patterns. (c) locations of the scale break across hydrodynamics as a function of normalized channel length. This test examines the impact of delta size bias. Nevertheless, these recalculated values are similar to those presented in the main text and do not impact our conclusions. Boxes in panels B and C indicate interquartile range (IQR, 75% - 25%), and lines inside the boxes are the medians. Whiskers and caps represent ±1.5× IQR**.**

Fig. S33.

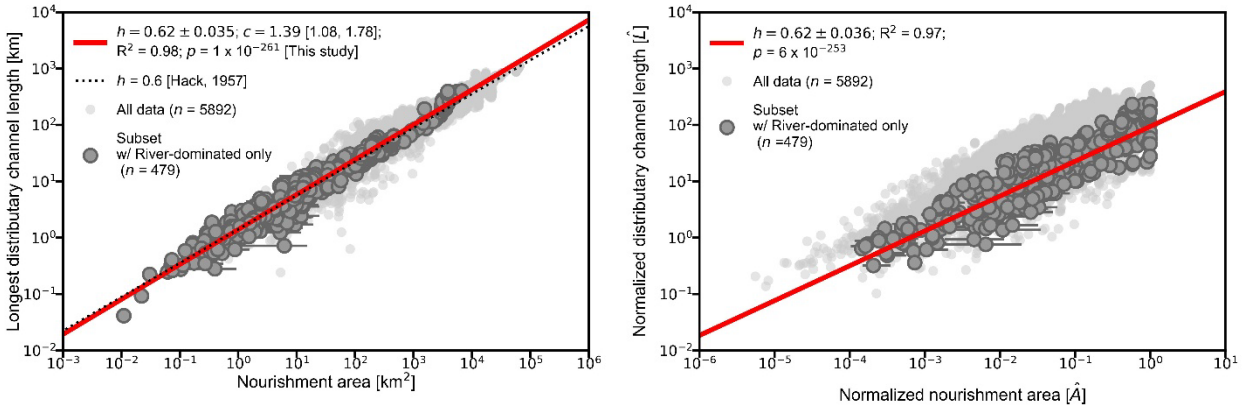

(left) Dimensional and (right) dimensionless scaling law of the distributary channel network of nourishment area (A) and the length (L) of the longest distributary channel in that area, obtained from the dataset of solely river-dominated deltas. R^2 and p-values are reported. Error bars represent the range of A, among 0×, 1×, and 2× local channel width (b), as shown in the buffer area boundary.

Fig. S34.

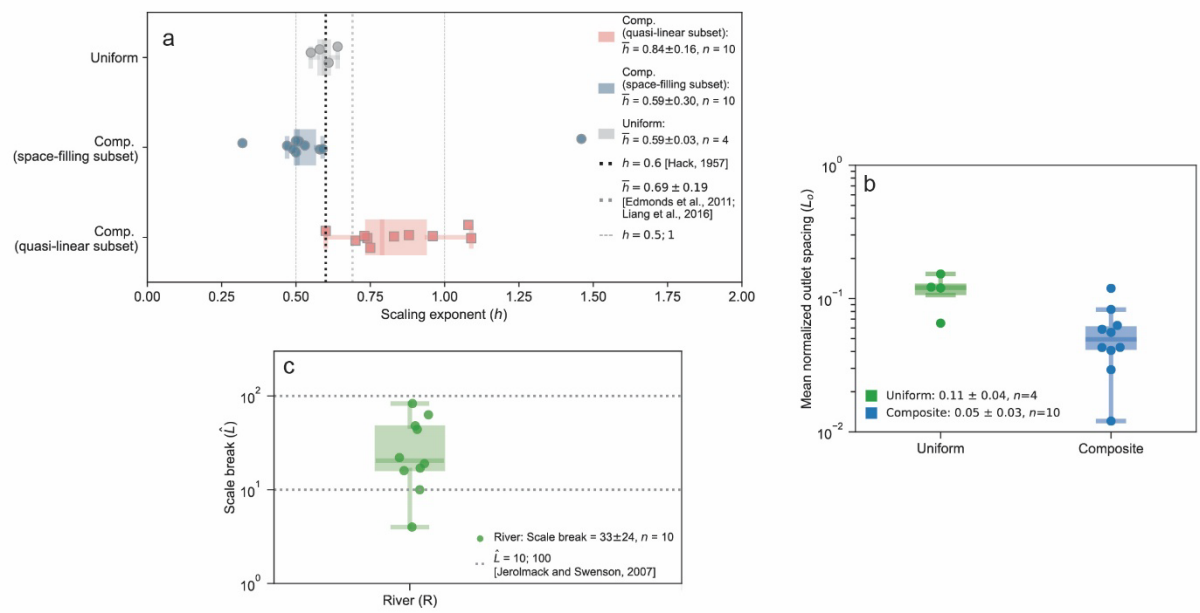

Recalculated plots corresponding to Figure 4A-C in the main text, using data from the river-dominated delta only, are presented here: (a) Scaling exponent h for the entire data set across different channel network patterns. n represents the amount of data. (b) Mean normalized outlet spacing (L_o) for river deltas with Uniform and Composite Network patterns. (c) locations of the scale break across hydrodynamics as a function of normalized channel length. This test is conducted to minimize the impact of marine influence on the delta network. Nevertheless, these recalculated values are similar to those presented in the main text and do not impact on our conclusions. Boxes in panels B and C indicate interquartile range (IQR, 75% - 25%), and lines inside the boxes are the medians. Whiskers and caps represent ±1.5× IQR**.**

Table. S1.

Reference	Type	Delta name	*n* in $A \sim L^n$	*h*	*s. dev. h*	*h* [this study]	*s. dev. h* [this study]	Sea level rise rate [mm/yr]	Sand fraction [%]	Resolution	Original source
Edmonds et al., 2011	Natural	Mossy Delta	1.89	0.53		0.63	0.10	-	~50	1m/pixel	National Geospatial-intelligence Agency
	Natural	Wax Lake Delta	1.91	0.52		0.58	0.08	-	~50-70	1m/pixel	U.S. Geological Survey Earth Explorer
	Flume Experiment	EM09	2.63	0.38		-	-	-	-	~mm	Hoyal and Sheets, 2009
	Numerical Model	Delft3D	1.98	0.51		-	-	-	50	25m/pixel	-
		Summary (i.e. mean)		0.48	0.06						
Liang et al., 2016	Numerical Model	DeltaRCM	1.07	0.93		-	-	0	25	50m/pixel	-
	Numerical Model	DeltaRCM	1.39	0.72		-	-	0	50	50m/pixel	-
	Numerical Model	DeltaRCM	1.45	0.69		-	-	0	75	50m/pixel	-
	Numerical Model	DeltaRCM	1.54	0.65		-	-	0	100	50m/pixel	-
	Numerical Model	DeltaRCM	1.07	0.93		-	-	0	25	50m/pixel	-
	Numerical Model	DeltaRCM	1.44	0.69		-	-	5	25	50m/pixel	-
	Numerical Model	DeltaRCM	1.46	0.68		-	-	20	25	50m/pixel	-
	Numerical Model	DeltaRCM	0.93	1.08		-	-	50	25	50m/pixel	-
		Summary (i.e. mean)		0.80	0.12						
		Combined Summary (i.e. mean)		0.69	0.19						

DeltaName	Apex width [m]"	h_1	h_1 ,95% CI	h_2	h_2 95% CI	Segm. R^2	Scale Break (sb)	sb 95% CI	h	h 95%	Orth. R_2	Delta Type^	L_o	Confinement*	Data Source`
Amazon	5200	0.83	0.05	0.68	0.05	0.89	59	25	-	-	-	RT	0.131	Confined	Landsat8
Colville	520	1.08	0.24	0.58	0.24	0.92	17	7	-	-	-	R	0.059	Unconfined	Landsat8
GBMD	890	0.86	0.04	0.55	0.04	0.96	58	7	-	-	-	RT	0.021	Confined One Side	Landsat5
Irrawaddy	820	0.76	0.05	0.35	0.05	0.91	157	16	-	-	-	RT	0.063	Confined One Side	Landsat8
Lena	6600	0.7	0.02	0.53	0.02	0.94	16	3	-	-	-	R	0.012	Unconfined	Landsat8
Mackenzie	2200	0.75	0.05	0.51	0.05	0.94	44	15	-	-	-	R	0.043	Confined	Landsat8
Mahakam	190	0.81	0.08	0.21	0.08	0.92	42	6	-	-	-	RT	0.062	Unconfined	Landsat5
Mahanadi	1300	0.8	0.06	0.25	0.06	0.89	201	22	-	-	-	RW	0.102	Unconfined	Landsat8
Mossy	4500	0.88	0.13	0.32	0.13	0.97	19	6	-	-	-	R	0.083	Unconfined	Landsat8
Niger	1320	0.72	0.05	0.49	0.05	0.94	68	24	-	-	-	R	0.063	Unconfined	Landsat8
Orinoco	2350	0.96	0.17	0.5	0.17	0.93	10	2	-	-	-	R	0.043	Confined One Side	Landsat8
Parana	1500	0.6	0.02	1.46	0.02	0.99	83	16	-	-	-	R	0.041	Confined	Landsat7
Red	1050	1.09	1.36	0.47	1.36	0.94	48	18	-	-	-	R	0.119	Unconfined	Landsat7
Selenga	800	0.73	0.06	0.49	0.06	0.98	22	8	-	-	-	R	0.056	Unconfined	Landsat8
Yukon	1350	0.83	0.14	0.59	0.14	0.93	4	2	-	-	-	R	0.029	Unconfined	Landsat5
Danube	860	-	-	-	-	-	-	-	0.65	0.11	0.83	RW	0.071	Confined	Landsat8
Dnieper	115	-	-	-	-	-	-	-	0.64	0.03	0.99	R	0.153	Confined	PlanetScope4
Fly	1100	-	-	-	-	-	-	-	0.66	0.12	0.8	RT	0.202	Confined	Landsat8
Hay	3200	-	-	-	-	-	-	-	0.54	0.14	0.99	RW	0.342	Unconfined	Landsat8
Kolyma	1700	-	-	-	-	-	-	-	0.73	0.04	0.9	RT	0.047	Confined	Landsat8
Krishna	960	-	-	-	-	-	-	-	0.58	0.19	0.94	RW	0.288	Unconfined	Landsat5
Mekong	370	-	-	-	-	-	-	-	0.55	0.06	0.86	R	0.122	Confined One Side	PlanetScope4
Mississippi	830	-	-	-	-	-	-	-	0.61	0.05	0.94	R	0.12	Unconfined	Landsat8
Pearl	270	-	-	-	-	-	-	-	0.64	0.04	0.88	RT	0.114	Confined	Landsat4
Po	370	-	-	-	-	-	-	-	0.52	0.19	0.94	RW	0.169	Unconfined	Landsat8
Rioni	370	-	-	-	-	-	-	-	0.76	0.18	0.96	RW	0.5	Unconfined	PlanetScope4
Wax	6400	-	-	-	-	-	-	-	0.58	0.08	0.91	R	0.065	Unconfined	Landsat5
Yangtze	5500	-	-	-	-	-	-	-	1.1	0.12	0.94	RT	0.335	Confined	Landsat8
Yenisei	3100	-	-	-	-	-	-	-	0.67	0.03	0.91	RT	0.054	Confined	Landsat8

*Prasojo et a.l, 2021, doi:10.1029/2021GL093656; Shaw et al., 2025, doi:doi.org/10.1130/B38386.1; Verified again visually from Google Earth images

^R-River, RT-River Tide, RW-River Wave (Nienhuis et al., 2020, doi:10.1038/s41586-019-1905-9; Vulis et al., 2023, doi:10.1029/2022GL102684)

`Schwenk et al., 2020, doi: 10.5194/esurf-8-87-2020; Hariharan et al., 2022, doi: https://doi.org/10.1029/2022GL097897

"measured from Google Earth

Table. S2.

Table. S3.

	Main Text	0x width buffer	1x width buffer	2x width buffer	Amazon & Colville as Uniform	Colville, Parana, Red as Uniform	w/o GBMD	w/o Lena	w/o GBMD & Lena	River-dominated
coefficient (overall)	1.43 [1.24, 1.65]	-	-	-	-	-	1.40 [1.17, 1.66]	1.38 [1.16, 1.65]	1.38 [1.15, 1.67]	1.39 [1.08, 1.78]
h (overall)	0.60±0.018	-	-	-	-	-	0.61±0.020	0.61±0.020	0.61±0.021	0.62±0.035
h_1 (quasi-linear)	0.83±0.13	0.76±0.13	0.79±0.12	0.91±0.22	0.81±0.12	0.80±0.07	0.83±0.13	0.83±0.13	0.83±0.13	0.84±0.16
h_2 (space-filling)	0.53±0.28	0.52±0.29	0.53±0.29	0.55±0.26	0.52±0.30	0.46±0.14	0.53±0.29	0.53±0.29	0.53±0.30	0.59±0.30
h (uniform)	0.66±0.14	-	-	-	0.67±0.13	0.66±0.13	0.66±0.14	0.66±0.14	0.66±0.14	0.59±0.03
$\hat{L}$ overall	62±60	50±53	53±51	66±65	-	-	-	-	-	-
$\hat{L}$ for River	33±24	-	-	-	33±25	25±19	33±24	33±25	33±25	33±24
$\hat{L}$ for River-Tide	78±46	-	-	-	86±51	78±46	84±52	78±46	84±52	-
L_o for uniform	0.18±0.13	-	-	-	0.16±0.24	0.16±0.24	0.18±0.13	0.18±0.13	0.18±0.13	0.11±0.04
L_o for composite	0.06±0.03	-	-	-	0.13±0.20	0.14±0.20	0.06±0.03	0.07±0.03	0.07±0.03	0.05±0.03

Data S1. (separate file and included herein as table S2)

Tabular data contains statistics of scaling relationships between distributary channel length and nourishment area for deltas used in this study (Figs 3, 4).

Data S2. (separate file)

Tabular data contains raw measurements, such as the distributary channel length used in this study (Fig. 2, figs. S2–S5).

Data S3. (separate file and included herein as table S1)

Tabular data contains the results of exponents (h) and the associated details about the river delta from past works.